Received: 7 April 2023 | Revised: 11 August 2023 | Accepted: 20 October 2023

DOI: 10.1049/rsn2.12505

IET Radar, Sonar & Navigation

The Institution of Engineering and Technology WILEY

ORIGINAL RESEARCH

High-resolution inverse synthetic aperture radar imaging of satellites in space

Simon Anger | **Matthias Jirousek** | **Stephan Dill** | **Timo Kempf** | **Markus Peichl**

German Aerospace Center (DLR) Microwaves and Radar Institute, Weßling, Germany

Correspondence
Simon Anger.
Email: simon.anger@dlr.de

Funding information
Federal Office of Bundeswehr Equipment, Information Technology and In-Service Support

Abstract

In view of the increasing number of space objects, comprehensive high-quality space surveillance becomes ever more important. Radar is a powerful tool that, in addition to detection and tracking of objects, also enables spatially high-resolution imaging independent of daylight and most weather conditions. Together with the technique of Inverse Synthetic Aperture Radar (ISAR), very high-resolution and distance-independent two-dimensional images can be obtained. However, advanced high-performance radar imaging of space objects is a complex and demanding task, touching many technological and signal processing issues. Therefore, besides theoretical work, the Microwaves and Radar Institute of German Aerospace Center (DLR) has developed and constructed an experimental radar system called IoSiS (Imaging of Satellites in Space) for basic research on new concepts for the acquisition of advanced high-resolution radar image products of objects in a low earth orbit. Based on pulse radar technology, which enables precise calibration and error correction, IoSiS has imaged space objects with a spatial resolution in the centimetre range, being novel in public perception and accessible literature. The goal of this paper is therefore to communicate and illustrate comprehensively the technological steps for the construction and successful operation of advanced radar-based space surveillance. Besides the basic description of the IoSiS system design this paper outlines primarily useful theory for ISAR imaging of objects in space, together with relevant imaging parameters and main formulae. All relevant processing steps, necessary for very high-resolution imaging of satellites in practice, are introduced and verified by simulation results. Finally, a unique measurement result demonstrates the practicability of the introduced processing steps and error correction strategies.

KEYWORDS
inverse synthetic aperture radar (ISAR), satellite imaging, space debris, space surveillance

1 | INTRODUCTION

Today, around 65 years after the launch of Sputnik 1, a globalised world without artificial satellites is no longer imaginable. The areas of application range from communication, navigation, remote sensing and weather satellites to the outpost of mankind on the International Space Station (ISS). Figure 1 shows the development of the number of objects classified by type since the beginning of the space age [1]. Right from the beginning, the number of functionless objects, that is, space debris, exceeds the number of operating satellites, that is, payloads. Additionally, within the last few years the number of unidentified objects has increased drastically. As a side note, the significantly higher number of smaller pieces of space debris estimated from the European Space Agency are not considered in the diagram shown. In addition, the rate of new satellites or spacecraft each year remained constant over decades until about 2010 [2]. Consequently, space situational awareness (SSA) played a secondary role, being driven mostly by military interest. Due to the start of the new millennium as

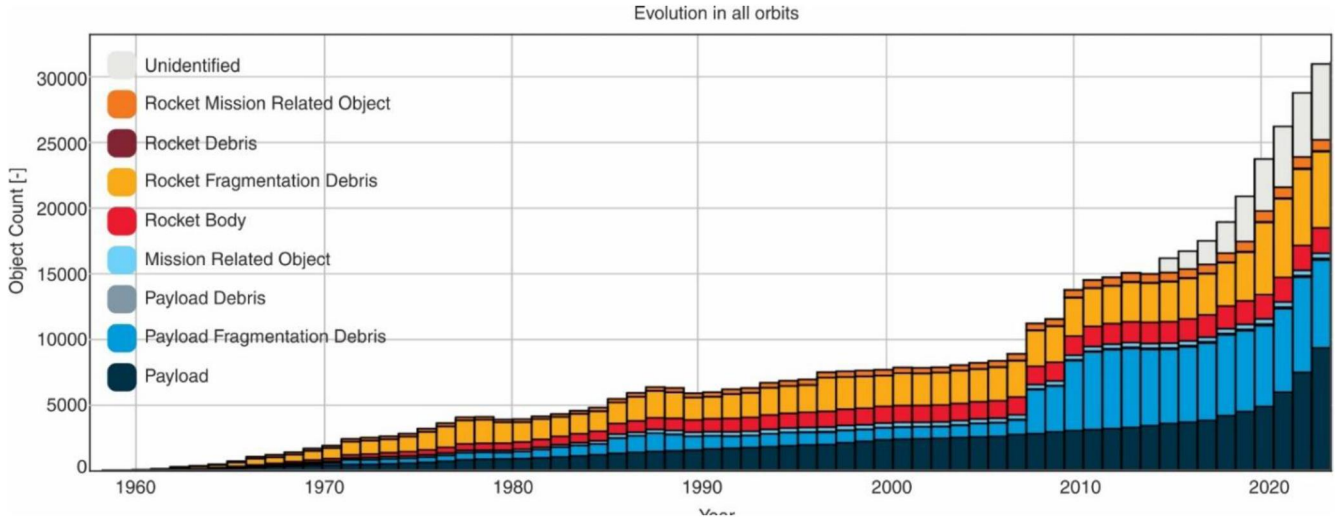

FIGURE 1 Number of regularly tracked space objects [1].

well as the beginning of the New Space era, the number of spacecraft and corresponding future space debris has increased dramatically since about 2010. New Space is the epoch where space technology is being heavily commercialised and has led to the founding of many startups that offer numerous new capabilities for spacecraft such as, payload, launch, operation and applications.

As a consequence, in addition to the detection and orbit determination, the detailed imaging of relevant space objects is similarly in great demand for space-using nations, because an unforeseeable failure of any system or just parts of it is directly associated with economic, financial and also qualitative losses. In order to detect or verify changes such as mechanical damage or deformation of a satellite system that could indicate a possible system failure at an early stage, a situation assessment can be performed using a highly resolved and detailed image of the object under investigation. ISAR imaging can also support the reentry event during deorbiting, where knowing the exact condition of the target is critical [3].

Thus, the ability to generate radar images from satellites with a very high spatial resolution can support the satellite surveillance, ensuring a trouble-free functioning of the operational satellite systems. Consequently, it is evident that, besides the classical military branches, army, air force and navy, new future battlefields will be or already have been built up in outer space. This new and completely different situation of outer space usage and corresponding harassment, either by space debris or a multitude of unidentified objects, requires breaking new technological ground for reliable and responsive SSA.

The USA operated its first radar for satellite imaging some 50 years ago [4, 5, 6]. Since then, the performance of these imaging systems has increased with the technological progress.

An overview of existing space surveillance radars for tracking and imaging can be found in [4, 7–14]. According to the public available information the known satellite imaging radars, like the HUSIR and TIRA systems as an example, use large dish antennas in a monostatic imaging geometry [7, 8]. Both are very high-performance radar systems with an imaging and tracking capability. However, they have so far been limited to a monostatic imaging geometry. Therefore, several years ago, the German Aerospace Center (DLR) started comprehensive theoretical analyses and the construction of an experimental radar system, called IoSiS—Imaging of Satellites in Space [15–18]. The research focus here is on imaging, which is why Imaging of Satellites in Space (IoSiS) does not yet have a tracking capability. The research with IoSiS supports the investigation of a future multifunctional radar-based imaging system with the idea of a new concept in satellite imaging. In contrast to existing systems, the concept envisages the use of a larger number of smaller, spatially distributed apertures that are suitable for bi- and multistatic as well as true three-dimensional images. A similar approach, intended for a planetary radar, using the concept of distributed antennas rather than a single large monolithic antenna, is described in [19].

The actual IoSiS system is an X-band radar providing a theoretical spatial resolution of up to 35 mm. It offers two receive channels by separated transmit and receive antennas and provides various operational modes using basically a pulse radar system architecture. This architecture enables the implementation of flexible, as well as, precise calibration and error correction procedures required for very high spatial resolution image processing. Furthermore, this architecture, together with fully digital signal generation, allows arbitrary transmit signals, which is unique in the field of SSA regarding publicly available information [4, 7–14].

The paper outlines in detail the following major topics:

- Basic signal theory,
- Processing steps,
- Design of a satellite imaging radar,
- Calibration procedure.

In addition, simulated imaging results with different spatial resolutions are presented, illustrating the expected capability of

the IoSiS imaging radar system, which then are verified by a measurement result of a real space object. In this way, the present work describes a working and validated way to develop and implement a radar for high performance imaging of low earth orbit (LEO) objects that can achieve centimetre-scale resolution.

2 | SIGNAL THEORY

This section derives a model of the measurement process and fundamental equations for spatial resolution and unambiguous range. Finally, the data processing method for high-resolution images is outlined [20, 21]. The described model assumes a non-manoeuvring/stable satellite, moving on a known trajectory. This is the case for most operational satellites, including the ISS, which are stabilised using control moment gyroscopes [22]. If the intrinsic motion is not known in advance, further algorithms have to be applied [23].

2.1 | Measurement model

A fixed ground-based radar system collects the data coherently along the satellite path in an ISAR geometry as depicted in Figure 2. For a point target p at a far-field distance $r = |\boldsymbol{r}|$ on the satellite we can determine the relation between the received electromagnetic field vector $\boldsymbol{E}_r$ and the transmitted field vector $\boldsymbol{E}_t$. The point target is described by the scattering matrix $\boldsymbol{S}$ which depicts the relation between the scattered field vector $\boldsymbol{E}_{\text{ref}}$ and incident field vector $\boldsymbol{E}_{\text{in}}$. With the wavenumber $k = 2\pi\lambda^{-1}$ the received radar data matrix for a single point target p can be expressed as

$$\boldsymbol{M}_{\text{P}}(\boldsymbol{r}_0, k) = \boldsymbol{S}(\boldsymbol{r}, k)\frac{e^{-\text{j}2kr}}{r^2}, \tag{1}$$

such that the received electric field yields

$$\boldsymbol{E}_r = \boldsymbol{M}_{\text{P}}(\boldsymbol{r}_0, k)\boldsymbol{E}_t. \tag{2}$$

The radar data $\boldsymbol{M}_{\text{P}}$ depends on the relative satellite position and the frequency which are indicated by $\boldsymbol{r}_0$ and k, respectively. Here $\boldsymbol{r}_0$ is the distance vector between the radar system and the centre of the satellite like indicated in Figure 2.

Especially in the case of ground-based imaging of satellites, this distance is considerably larger than the dimension of the target. Hence, we can apply a far-field approximation and can express the distance r by the scalar product $\boldsymbol{re}_0$, where $\boldsymbol{e}_0$ is the unit vector in direction of $\boldsymbol{r}_0$.

This corresponds to a Taylor series expansion with termination according to the linear term [24]. If we additionally neglect the electromagnetic interaction between different point scatterers of the whole satellite, the radar data for s_{tot} point targets can be expressed as

$$\boldsymbol{M}(\boldsymbol{r}_0, k) = \sum_{n=0}^{s_{\text{tot}}} \boldsymbol{S}(\boldsymbol{r}_n, k)\frac{e^{-\text{j}2k\boldsymbol{r}_n\boldsymbol{e}_0}}{r_n^2}. \tag{3}$$

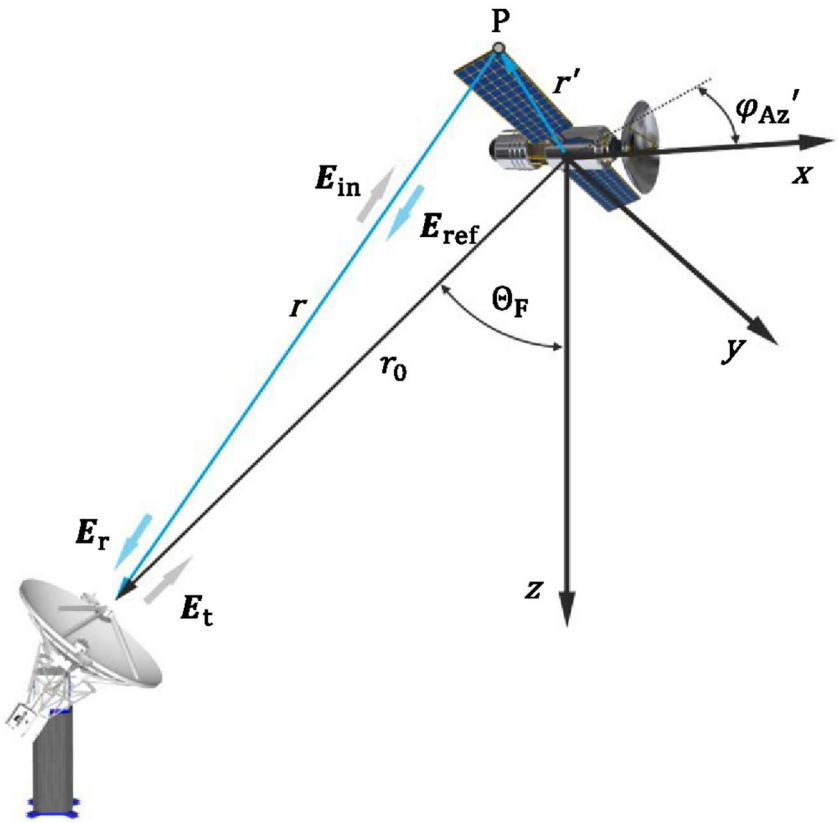

FIGURE 2 Inverse synthetic aperture radar imaging geometry of a ground-based satellite imaging radar system.

In the next step the vector $\boldsymbol{r_n}$ which represents the distance between the sensor and the nth point scatterer location can be expressed with $\boldsymbol{r_n} = \boldsymbol{r}_0 - \boldsymbol{r}'_n$ corresponding to Figure 2. With $\boldsymbol{e}_0\boldsymbol{r}_0 = r_0$ we can write:

$$\boldsymbol{M}(\boldsymbol{r}_0, k) = \frac{e^{-\mathrm{j}2kr_0}}{r_0^2} \sum_{n=0}^{s_{\mathrm{tot}}} \boldsymbol{S}(\boldsymbol{r}'_n, \boldsymbol{e}_0, k)\, e^{\mathrm{j}2k\boldsymbol{r}'_n\boldsymbol{e}_0}. \tag{4}$$

here the phase term $e^{-\mathrm{j}2kr_0}$ is independent from the point scatterer locations and constitutes a phase offset for all scatterers in the target scene. However, considering IoSiS with a ground-based radar system the distance $|\boldsymbol{r}_0|$ varies depending on the current satellite position. This translational motion dr_0/dt is the same for every point target and gives each scatterer the same Doppler shift. Hence this phase offset is not useful for the ISAR imaging process and has to be corrected later in the image processing procedure [25].

For the representation of the measurement data in the spatial frequency domain we substitute $\boldsymbol{p} = 2k\boldsymbol{e}_0$ and with $p = 4\pi f/c$ we get:

$$\boldsymbol{M}(\boldsymbol{r}_0, \boldsymbol{p}) = \frac{e^{-\mathrm{j}pr_0}}{r_0^2} \sum_{n=0}^{s_{\mathrm{tot}}} \boldsymbol{S}(\boldsymbol{r}'_n, \boldsymbol{e}_0, p)\, e^{\mathrm{j}p\boldsymbol{r}'_n}. \tag{5}$$

This representation of the measurement data in the spatial frequency domain is illustrated in Figure 3. In the case of the radar measurement bandwidth B, the corresponding spatial frequency is $\Delta p = 4\pi B/c_0$. The radar centre frequency f_c is represented by $p_c = 4\pi f_c/c_0$. Assuming Δp and p_c along with the azimuth integration angle $\Delta\varphi_{\mathrm{Az}}$, the measured radar data represent a sector of an annulus. The integration angle $\Delta\varphi_{\mathrm{Az}}$, determining the azimuth resolution, is determined through the angular change of the line of sight between the radar and the target satellite which in turn is represented by the vector $\boldsymbol{r}_0$. This, together with Figure 3, shows that the measured data M can be expressed using the dependencies $\Delta\varphi_{\mathrm{Az}}$ and p, which allows us to write

$$\boldsymbol{M} = \begin{bmatrix} \boldsymbol{U}(\varphi_{\mathrm{Az},1}, p_1) & \cdots & \boldsymbol{U}(\varphi_{\mathrm{Az},1}, p_l) \\ \vdots & \ddots & \vdots \\ \boldsymbol{U}(\varphi_{\mathrm{Az,m}}, p_1) & \cdots & \boldsymbol{U}(\varphi_{\mathrm{Az,m}}, p_l) \end{bmatrix}, \tag{6}$$

with

$$\boldsymbol{U}(\varphi_{\mathrm{Az,m}}, p_l) = \frac{e^{-\mathrm{j}p_l r_0}}{r_0^2} \sum_{n=0}^{s_{tot}} \boldsymbol{S}(\boldsymbol{r}'_n, \varphi_{Az,m}, p_l)\, e^{\mathrm{j}\boldsymbol{r}'_n\boldsymbol{p}}. \tag{7}$$

The summation still represents the superposition of s_{tot} single point scatterers. The matrix in Equation (6) represents the imaging aperture in the spatial frequency domain which is defined by the radar system bandwidth in range direction and by the integration angle in azimuth direction.

2.2 | Spatial resolution and unambiguous range

The arrangement of the ISAR measurement data in the spatial frequency domain, described by Equation (5), is illustrated in Figure 3 along with its projection in the p_xp_y plane. By projection of the spatial frequency spectrum the p_xp_y plane is chosen as focal plane. In satellite imaging, it can be beneficial to choose a focal plane dependent on the three-dimensional structure and orientation of the imaged satellite instead of

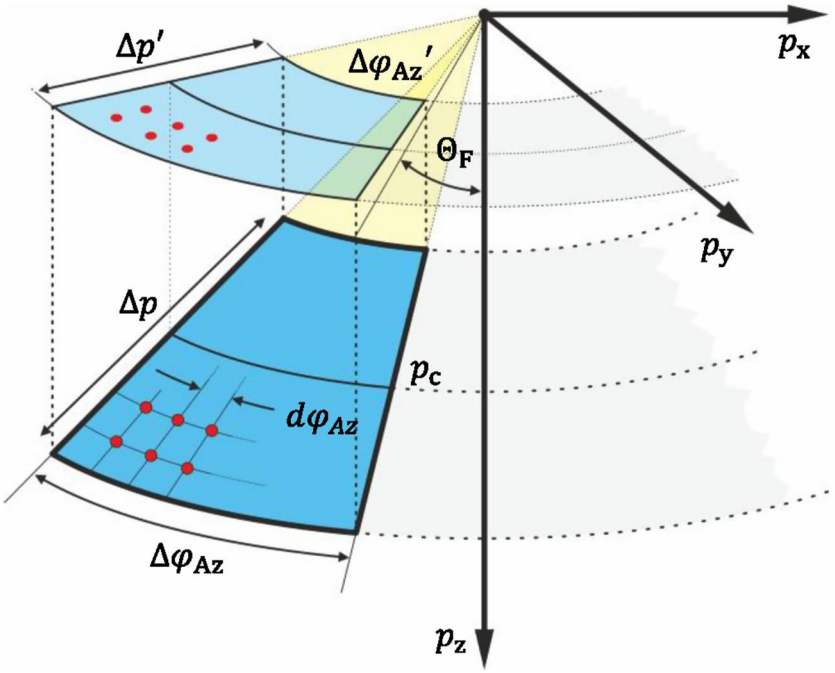

FIGURE 3 Arrangement of the inverse synthetic aperture radar measurement data in the spatial frequency domain together with the projection in the p_x-p_y plane resulting in a sector of an annulus.

choosing the slant range as focal plane. Otherwise distortions could degrade the radar image. But, according to the illustrated projection, the spatial frequency bandwidth Δp is clinched to $\Delta p'$ with the relation $\Delta p' = \Delta p \bullet \sin\theta_F$. This results in a degradation of the spatial resolution in the final radar image by a factor $1/\sin\theta_F$.

The angular step size $d\varphi_{Az}$ is the sample interval of the spatial azimuth frequency and is determined by the pulse repetition frequency (PRF) of the radar system, in conjunction with the angular velocity of the satellite. By considering the orbital dynamics of the satellite's trajectory relative to the radar position, it follows that the angular sampling interval is not constant due to the changing angular speed. The highest angular speed and thus the largest values for $d\varphi_{Az}$ arises at zenith, that is, at an elevation angle of 90°. However, high elevation passes of satellites in the vicinity of the zenith are the exception rather than the rule.

Using the representation of the radar data in the spatial frequency domain, we can derive the achievable spatial resolution in azimuth direction. This resolution is determined by the spatial frequency bandwidth Δp_{Az} which can be estimated for small azimuth angles [26]:

$$\Delta p_{Az} = 2p_c \cdot \sin\left(\frac{\Delta\varphi_{Az}}{2}\right). \tag{8}$$

Applying the general relation between the spatial resolution and the bandwidth $\Delta r = c_0/2B$ we can express the azimuth resolution as

$$\Delta r_{Az} = \frac{c_0}{2B} = \frac{4\pi}{c_0}\frac{c_0}{2\Delta p_{Az}} = \frac{c_0}{4 \cdot f_c \cdot \sin\left(\frac{\Delta\varphi_{Az}}{2}\right)}. \tag{9}$$

The azimuth resolution depends on the radar centre frequency f_c as well as the synthesis angle $\Delta\varphi_{Az}$ in azimuth direction. As seen from Equation (9), the higher the radar frequency, the better the achievable azimuth resolution, assuming a constant angle $\Delta\varphi_{Az}$. This can be explained by the fact that at higher transmit frequencies, and the associated smaller wavelengths, a faster phase change in the azimuth signal can be achieved which results in a higher azimuth bandwidth and a higher azimuth resolution. It is well known that in an ISAR system a larger azimuth angle results in a better azimuth resolution when it is assumed that the individual scattering centres provide a measurable amplitude contribution over the entire angular range under consideration. However, this is not the case with real target objects in connection with very large angular ranges. That is why the azimuth resolution is constrained to certain limits given by the angular-restricted backscatter properties of the satellite. In principle, this problem can be counteracted by increasing the radar transmit frequency to achieve a high azimuth resolution at smaller synthesis angles. But now, further restrictions have to be considered such as high atmospheric attenuation or more difficult transmit power generation at high frequencies for instance.

In addition to the spatial resolution, the scene width is of particular interest in both, range and azimuth direction, for which an unambiguous image is guaranteed. In azimuth direction this unambiguous range is determined by the width of the sampling interval $d\varphi_{Az}$. To illustrate this, consider a remote sensing SAR satellite for earth observation. Here, we have to choose the length of the unambiguous range according to the foot print of the antenna beam on the earth's surface. Thus, the necessary unambiguous range depends mainly on the radar antenna characteristics in this case. For the reverse case of ground-based satellite imaging the necessary unambiguous range depends only on the size of the satellite since it can be assumed that only reflections from the satellite structure contribute to the received signal because the background is empty space. If we use the sampling interval $d\varphi_{Az}$ in Equation (9) instead of the synthesis angle $\Delta\varphi_{Az}$, the unambiguous range in azimuth direction can be expressed as

$$A_{Az} = \frac{c_0}{4 \cdot f_c \cdot sin\left(\frac{d\varphi_{Az}}{2}\right)}. \tag{10}$$

With the pulse repetition interval (PRI) and the angular velocity ω_{Az} of the satellite, with respect to the radar system, the sampling interval can be determined and expressed as $d\varphi_{Az} = \omega_{Az} \cdot \mathrm{PRI}$. Thus, the PRI has to be high enough to guarantee a sufficient unambiguous range in azimuth direction.

As the centre frequency increases, the unambiguous range consequently decreases. Thus, in order for the unambiguous range to remain constant, the spatial frequency spectrum must be sampled more finely. This can be explained by the fact that the higher frequency and the associated faster phase change in the azimuth direction also result in higher spatial frequencies which, according to the Nyquist theorem, must be sampled at a correspondingly higher rate.

2.3 | Image formation

Equation (5) shows the basic Fourier relationship between the data in the image domain and the data measured in the spatial frequency domain. However, since the measurement data in the ISAR case are arranged on a polar grid, they cannot simply be mapped into the image domain using a fast Fourier transformation, since this would require a rectangular sampling grid. The Range-Doppler algorithm approximates this polar grid for small azimuth observation angles by just assuming a Cartesian grid. It is well known, that this is no longer valid for increasing observation angles and would lead to defocusing effects in the ISAR image and hence to a degradation of the azimuth resolution.

The correlation method [21] represents the most exact solution of the back calculation between the measured raw radar data $\boldsymbol{M}$, described in Equation (6), and the complex reflectivity distribution $\boldsymbol{S}$ ($\boldsymbol{r}'$) in the target area, and can expressed as:

$$\boldsymbol{S}(\boldsymbol{r}') = \sum_{m=1}^{n_{\mathrm{Az}}} \left\{ r_0^2 \sum_{l=1}^{n_{\mathrm{p}}} \left(e^{\mathrm{j}p_l r_0} [\boldsymbol{M}]_{m,l}\, e^{-\mathrm{j}p_l \Delta r} \right) \right\}, \qquad (11)$$

and $\Delta r = |\boldsymbol{r}_0| - |\boldsymbol{r}| = r_0 - r$ according to Figure 2. Furthermore $n_{\mathrm{Az}} = \Delta\varphi_{\mathrm{Az}}/\mathrm{d}\varphi_{\mathrm{Az}}$ is the total number of samples in azimuth direction and n_{p} is the number of spatial frequencies used. The image generation or focussing of each pixel is carried out by the coherent summation of the raw radar data for each individual pixel, where every image pixel depends on each complex sampling point in the spatial frequency range. Using the coordinates of the position vector of each pixel, there are four loops for the direct implementation of this image reconstruction method and thus a considerable computational effort is required. Since the computational effort can only be reduced at the expense of the accuracy in image generation, that is, certain approximations, an acceptable compromise has to be found.

The back-projection algorithm (BP) for ISAR image reconstruction represents such an approximation of the correlation method [27]. However, the BP allows the result of the correlation method to be approximated with any degree of accuracy by variable adjustment of the number of image pixels and therefore of the computational effort. The BP is based on the Fourier transform projection theorem, which states that the Fourier spectrum $F_{\mathrm{p}}(f_x)$ of a two-dimensional function $f(x,y)$ projected on the x axis is equal to the intersection of the two-dimensional Fourier transform $F(f_x f_y) \bullet\!\!-\!\!\circ f(x,y)$, along the x axis. Here the x axis is arbitrarily chosen as the projection line.

Applying this theorem to the special case of a radar system that illuminates a scene in defined angular steps results in a range profile that corresponds to the projection of a two-dimensional function (target area) onto the projection line defined by the viewing angle of the radar system.

The BP now solves the image generation described by Equation (11) in two steps. In the first step, the inner summation gives the projected two-dimensional target area in the form of the one-dimensional, angle-dependent range profile $\boldsymbol{H}(\varphi_{\mathrm{Az}},\Delta r)$. The mth range profile can be expressed as

$$\mathbf{H}\left(\varphi_{\mathrm{Az,m}}, \Delta r\right) = r_0^2 \sum_{l=1}^{n_p} e^{\mathrm{j}(p_l - p_c) r_0} [\boldsymbol{M}]_{m,l} e^{-\mathrm{j}(p_l - p_c)\Delta r}. \qquad (12)$$

In case of using a frequency modulated pulse radar, the measurement data is sampled directly in the time domain, thus the range profiles are already available at the output of the matched filter in the image domain. But in this case, the signal still has to be corrected with the complex phase term $e^{\mathrm{j}pr_0}$ in the spatial frequency range. This phase term performs the range correction corresponding to the mean distance $|\boldsymbol{r}_0|$ to the satellite at every single azimuth position, and centres the range profiles in the image domain around the image coordinate zero. In this way the distance to the centre of the space object, which varies in range across the synthetic aperture (SA), will be compensated.

In the second step, the available range profiles are coherently projected onto a given two-dimensional grid and summed up. The coordinates of each individual pixel in this grid are defined by $\boldsymbol{r}' = [x_n, y_m]$. The plane in which this grid is placed is called the focus plane. A target scene, in this case the satellite structure, consisting of scattering centres arranged in three-dimensional space is thus projected onto this two-dimensional target grid. This superposition of all range profiles results in the focussing of the ISAR image in the azimuth direction. Equation (13) describes the coherent projection of the single range profiles onto the grid to obtain the two-dimensional reflectivity map $\boldsymbol{S}(\boldsymbol{r}')$ of the satellite.

$$\boldsymbol{S}(x_n, y_m) = \sum_{m=1}^{n_{Az}} e^{\mathrm{j}p_c r_0} \mathbf{H}\left(\varphi_{\mathrm{Az,m}}, \Delta r\right)\, e^{-\mathrm{j}p_c \Delta r}. \qquad (13)$$

The phase term $e^{-\mathrm{j}p_c\Delta r}$ corrects the phase information of the single range profiles depending on the centre frequency and the spatial position of the sensor relative to the corresponding image pixel. The second phase term $e^{-\mathrm{j}p_c r_0}$ compensated the mean phase shift of the radar to the centre of the satellite. The phase terms are within the summation because r_0 and Δr both depend on the azimuth angle φ_{Az} (The distance $|\boldsymbol{r}_0|$ to the satellite varies along the SA). Both terms together ensure the coherent summation of the range profiles on the image grid. The extent and number of points of the grid can be selected on demand. However, the number of points per area segment should be sufficiently larger than the number of resolution cells in this area segment. Experience has shown, that four image pixels per resolution cell result in proper imaging quality.

3 | OPERATIONAL PARAMETERS

In the following, the fundamental radar parameters PRF, unambiguous range and spatial azimuth resolution are determined.

A basic requirement for proper ISAR imaging is sufficiently high sampling of the target area in the azimuth direction in order to obtain an adequate large unambiguous range and thus avoid aliasing effects in the azimuth direction. The necessary size of the unambiguous range in azimuth direction can be determined in remote sensing, such as radar earth observation for instance, based on the area that is illuminated by the antenna footprint. For an antenna pointing to the sky, it can be assumed that only the object to be imaged is within the antenna main beam. Therefore, no reflections from the environment or background are present which could interfere with the radar image in case of insufficient sampling in azimuth direction. As a result, the necessary size of the azimuth unambiguous range depends only on the size of the space object. The unambiguous range can be determined using the angle increment and the transmission frequency. Thus, at a given transmission frequency, the PRF together with the angular velocity of the space object determines the unambiguous cross range that can be achieved. Since the orbital velocity and thus also the angular velocity is given, the PRF has to be selected depending on the size of the space object. Following this approach, we assumed that the corresponding space object does not exhibit any significant self-rotation but remains aligned with the centre of gravity of the earth (e.g. attitude control). In the case of self-rotation, the PRF may have to be selected to be larger because of the higher angular velocity.

The angular velocity as a function of the elevation angle for different orbital heights of the space object is illustrated in Figure 4. The angular velocity is depicted for a satellite pass with a maximum elevation angle of 90° (zenith pass), as well as for a satellite pass with a maximum elevation angle of 50°. The highest angular velocities occur at high elevation passes. However, the angular velocity decreases as the orbital height increases or the elevation angle decreases, respectively. Considering a zenith pass, the angular velocity is just above 1°/s at an orbital altitude of 400 km, and reduces to 0.15°/s at an orbital altitude of 2000 km. The decrease is due to the fact that, on the one hand, the orbital speed of a space object decreases with increasing orbital height, and on the other hand, the space object has to travel a larger distance at higher orbital heights for the same azimuth angle [28].

Since a direct overflight through the zenith rarely occurs in practice, the angular velocities for a typical overflight with a maximum elevation angle of 50° for different orbit heights are also shown for comparison.

In this case, the angular velocity decreases as well, as the orbit height increases. Compared to the zenith pass, however, the maximum angular velocity at an orbit altitude of 400 km is somewhat lower at 0.8°/s. Since the orbital height of the majority of the satellites orbiting the earth is more than 400 km, the upper limit of the angular velocity and the unambiguous range can be determined depending on the PRF of the radar system.

Figure 5 shows the unambiguous range for maximum values of the angular velocity (taken from Figure 4 at an elevation angle of 90°) as a function of the PRF for different orbital heights and a centre frequency of the radar system of 11 GHz (X band). Corresponding to the decreasing angular velocity, the unambiguous range increases using a constant PRF together with an increasing orbital height. At a PRF of 50 Hz for instance, the unambiguous range is 38 m at an orbital height of 400 km, and increases to about 260 m at an orbital height of 2000 km.

Considering the extent of satellites currently orbiting Earth in LEO, these sizes of the unambiguous range would be sufficient, with the exception of the ISS. Even with the knowledge that the current trend is towards smaller satellites (small, micro, nanosatellites), these values would be sufficient. However, with regard to the imaging of the ISS, which has a very low orbital altitude with a zenith distance of about 400 km, a higher PRF is necessary in X band. The dimensions of the ISS are approximately 110 × 90 m, which is currently by far the largest object in LEO.

Based on a transmit frequency of 11 GHz, PRF values of around 200 Hz are necessary for the ISS, which leads to an unambiguous range of around 150 m. Thus, in the following, a PRF in the range of 200 Hz is selected for both the simulations and the measurements described later. It should also be noted that when choosing the PRF, the achievable signal-to-noise ratio (SNR) also plays a non-negligible role, since the coherent integration over the pulses, in which a scattering centre still makes a significant contribution, produces gain in the SNR.

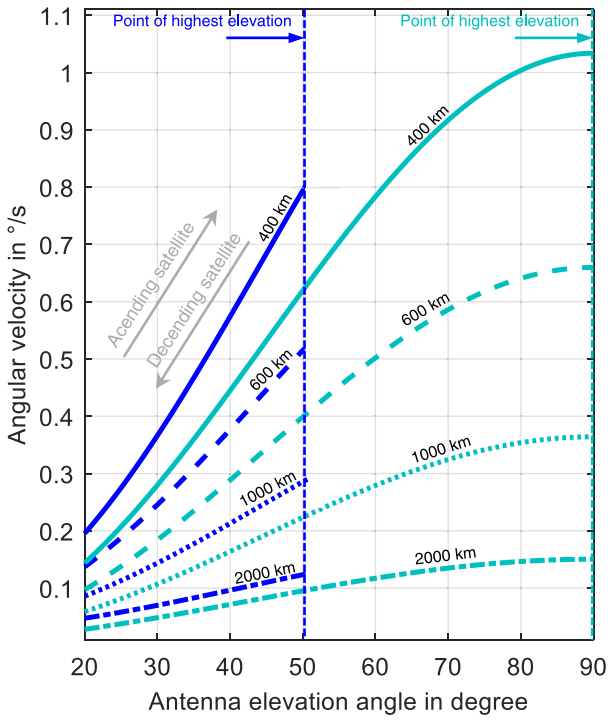

FIGURE 4 Angular velocity in azimuth direction as function of the antenna elevation angle for different orbital heights for a satellite pass with a maximum elevation angle of 50° (blue) and for a pass with a maximum elevation angle of 90° (Zenith, cyan).

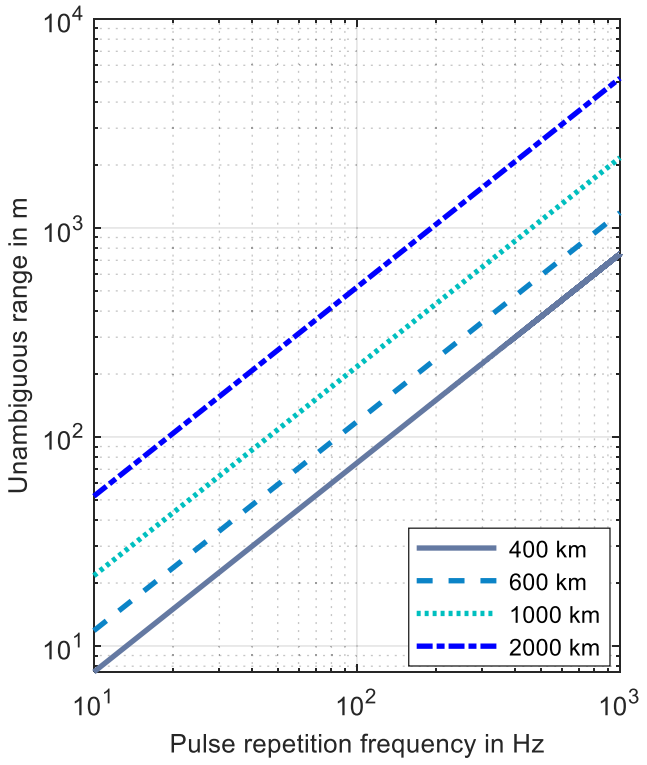

FIGURE 5 Azimuth unambiguous range for different orbit heights as function of the pulse repetition frequency.

The course of the phase history seen across the range profiles can also be better resolved at higher pulse repetition frequencies, which is very helpful in anticipation of necessary error corrections. Therefore, it generally makes more sense to choose a large as possible PRF. However, often the PRF is limited by hardware constraints. For instance, In the case of IoSiS, the maxim achievable data rate of the analogue-to-digital converters together with the timing unit used limits the PRF to about 200 Hz.

A fundamental system parameter of an imaging radar system is the used frequency range. Depending on the area of application of the imaging radar system, there are criteria that limit the selection of a suitable frequency range. Considering radar remote sensing, these areas are the transmission windows, where the attenuation of the atmosphere shows local minima [29]. Although higher frequencies involve higher signal attenuation there are also advantages in the use of higher radar transmit frequencies. One of the key benefits associated with ISAR at higher frequencies is the reduction of the necessary azimuth integration angle for high-resolution imaging. Furthermore, the X band, in which IoSiS works, is not suitable for long-term operational use due to the multiple occupancy of the frequency band by communication and other radar systems. Thus, in parallel with the experiments in X band, theoretical investigations on three further suitable frequency bands were also made. Figure 6 shows the unambiguous range for all four assumed radar transmit frequencies (11 GHz/X band, 35 GHz/Ka band, 96 GHz/W band, 142 GHz/D band) as a function of the PRF.

In accordance with the smaller wavelength at higher frequencies and the associated requirement for finer sampling, the unambiguous range decreases with the pulse frequency remaining the same, while the centre frequency of the radar increases at the same time.

However, it can be observed that at all assumed radar centre frequencies for a PRF of 200 Hz, an unambiguous range of around 10 m can be achieved. With the exception of the ISS, this is sufficient for imaging most satellites in LEO.

The theoretically achievable spatial resolution in azimuth direction is depicted in Figure 7 as a function of the integration angle for different radar centre frequencies. Also shown is the equivalent system bandwidth that is necessary to obtain the same spatial resolution in range direction. The two image quality parameters, range and azimuth resolution, are considered together here, since it is convenient for better image interpretation that these two system parameters are approximately the same size. According to (9) the azimuth resolution improves linearly as the radar centre frequency increases. An important requirement for achieving the specific azimuth resolution is, that the individual scattering centres make a significant contribution over the whole angular range. Thus, scattering centres which have strong angle-dependent radar cross-section (RCS), cannot be focused with the theoretical maximum spatial resolution. Considering a scatterer whose angularly limited backscatter behaviour allows an integration angle of 4°, for instance, a radar centre frequency of 11 GHz can achieve a maximum resolution

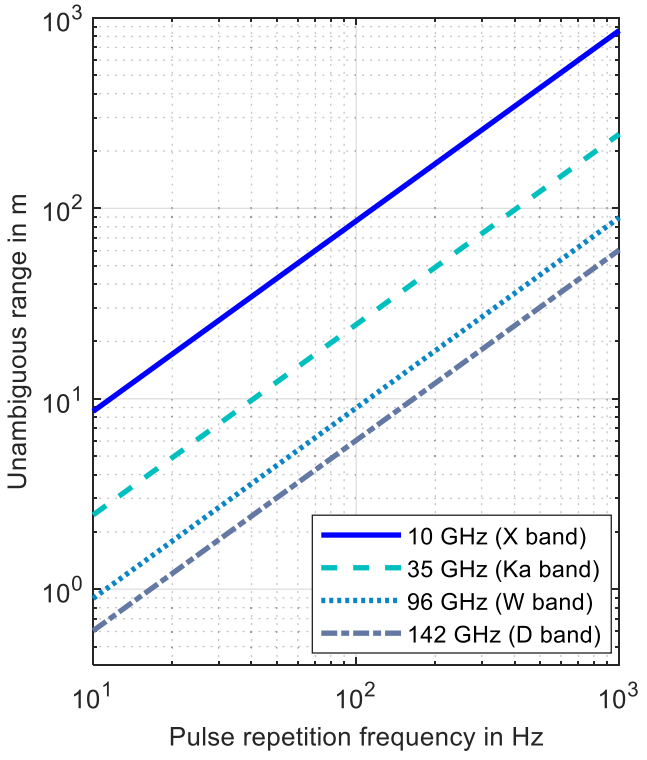

FIGURE 6 Azimuth unambiguous range for different radar centre frequencies as function of the pulse repetition frequency.

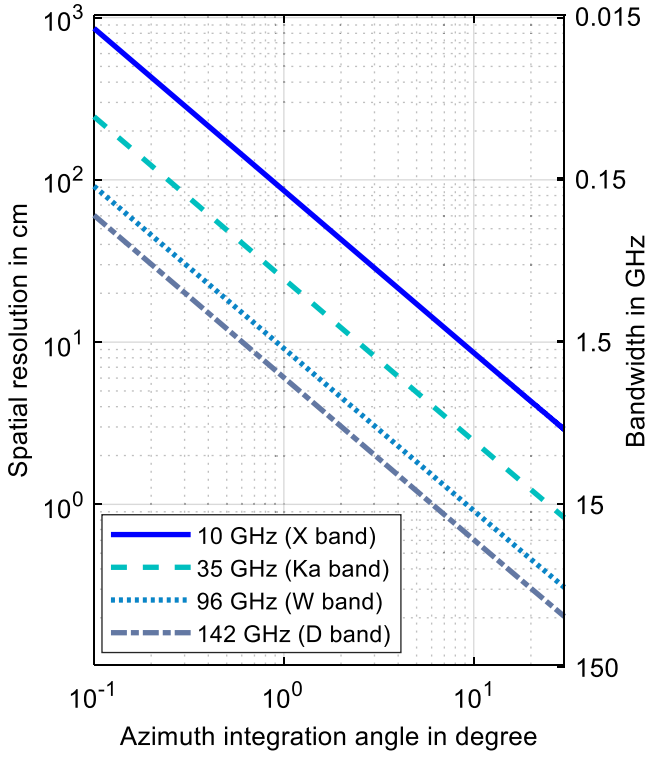

FIGURE 7 Spatial azimuth resolution as function of the integration angle for different radar centre frequencies. In addition, the equivalent bandwidth is depicted, being required to achieve a quadratic resolution cell.

in the azimuth direction of 20 cm. At 80 GHz this maximum achievable resolution is already 2.7 cm.

In terms of azimuth resolution, this represents a significant advantage of high radar centre frequencies over lower frequencies in several respects. On the one hand, scattering centres whose backscatter behaviour is angularly limited, can also be imaged with the highest resolution. On the other hand, whenever a satellite is imaged using a large azimuth angle range, not only one ISAR image with high spatial resolution can be obtained, but several. This allows the generation of ISAR movies. This time series imaging may allow the extraction of more information about an unknown object. For example, an unnatural movement (such as a tumble) of the whole object or part of it, provided that this unknown intrinsic movement is not too fast and still allows the image to be focused. Moreover, time series imaging in the azimuth direction is beneficial to capture not only the azimuth resolution but also as many scattering centres of the space object as possible, which increases the information content of the radar image.

4 | THE IoSiS RADAR SYSTEM

For the validation of the theoretical results and the experimental investigation of new radar imaging concepts, an experimental radar system was developed and constructed at the DLR satellite ground station in Weilheim, Germany [15, 20, 30] (see Figure 8).

4.1 | System design

The stationary ground-based radar system uses a steerable antenna to track a space object during its orbital pass. However, if a tracking radar is not available, the orbit of the object of interest must be predicted before each measurement. Firstly, a large azimuth integration angle, that is, a large SA, is desirable to get a high azimuth resolution. Secondly, this range of observation angle provides as much coherently integrated radar backscatter as possible from the space object, which would not be available for small angle ranges.

Figure 9 shows a sketch of the main components of IoSiS. It consists of a steerable reflector antenna system with a 9 m diameter transmit (Tx) antenna in a Cassegrain configuration and two separated directly fed receiving (Rx) antennas together with the radar electronics in a close-by container. Both receive antennas have a diameter of 1.8 m. So far, the measurement results discussed in this paper are based on only one receiving channel. The second receive antenna or channel, respectively, is planned for future multi-channel imaging studies.

In present implementation of the IoSiS system, the DLR advanced multi-purpose X-band radar system GigaRad is used [31, 32]. The Tx channel of the radar is connected to a high-power amplifier (HPA) located on the rear side of the main dish, which itself feeds the feed horn via rectangular waveguide. Thus, the Cassegrain antenna configuration allows a short and low loss connection between the HPA and the antenna feed. The Rx antennas are connected via low-noise amplification and optical cabling to both Rx channels of GigaRad. Table 1 shows basic system parameters of the IoSiS radar as used for ISAR imaging operation. Here the maximum possible instantaneous bandwidth allows range resolution up to 35 mm. Presently the PRF is limited to 200 Hz. However, a new timing unit, currently under development, will enable a varying PRF with more than one travelling pulse per round trip time and hence an increased PRF.

4.2 | Calibration procedure

In order to achieve the nominal performance of the imaging system in terms of spatial resolution as well as radiometric

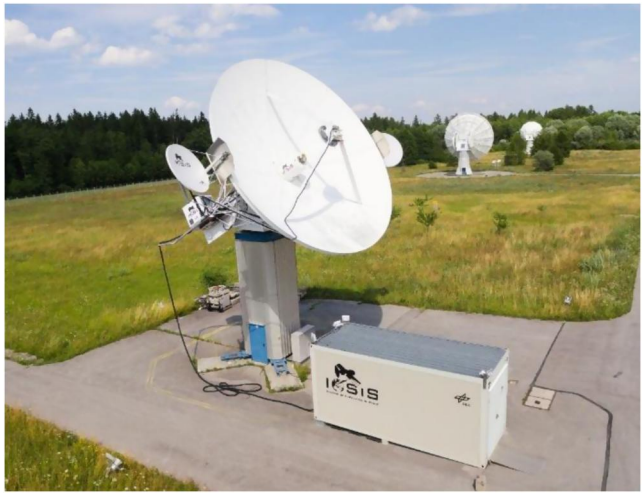

FIGURE 8 Photograph of the experimental imaging of satellites in space radar system (IoSiS), installed at Weilheim facilities of DLR, Germany.

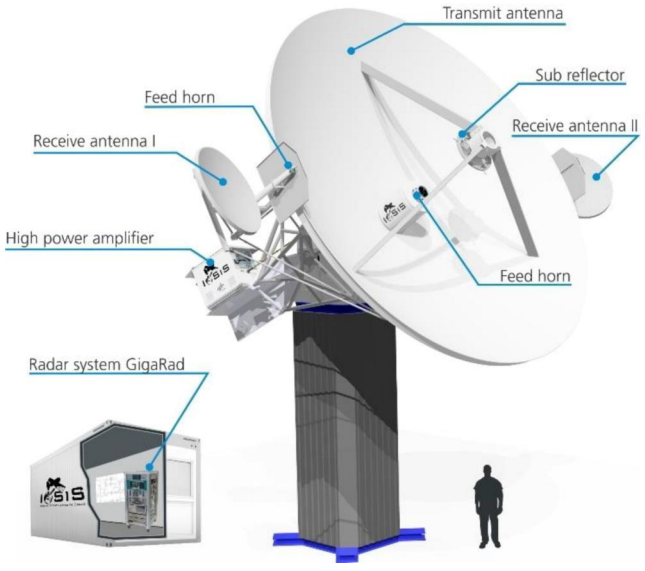

FIGURE 9 The imaging of satellites in space system with its 9 m transmit antenna and two 1.8 m receive antennas. The main radar electronics is located in a nearby container.

sensitivity (SNR), the correction of the non-ideal system transfer function is necessary.

The determination and correction of the system transfer function is carried out in two steps for the IoSiS system. First, the system transfer function of the radar electronics is determined on its own. To achieve this, a calibration network is implemented allowing the acquisition of calibration pulses before and after the measurement. With $H_t(f)$ as the transfer function of the transmit path, $H_r(f)$ for the receiving path and $H_{cal}(f)$ for the calibration path, the received signal results in.

$$S_{c_{Ra}}(f) = S_{ref} \cdot H_t \cdot H_r \cdot H_{cal}. \tag{14}$$

Here S_{Ref} is the reference signal, being for instance a chirp signal. Now we can determine the calibration filter function to mitigate the influence of the transmit and receive path of the radar, being

$$C_{ra}(f) = (H_t \cdot H_r)^{-1} = \frac{S_{ref} \cdot H_{cal}}{S_{c_{ra}}}. \tag{15}$$

If the calibration path H_{cal} is sufficiently characterised in advance it can be mitigated.

In a second step the influence of the antenna system, including the feed network, is considered based on a calibration measurement using a ground-based reference target like a corner reflector. This measurement is done only once, because it can be assumed that the antenna transfer function remains constant over time. With $H_{t_{ant}}$ and $H_{r_{ant}}$ being the transfer function of the transmit and receive antenna components, respectively, we get

$$S_{c_{ant}}(f) = S_{ref} \cdot H_t \cdot H_{t_{ant}} \cdot H_{target} \cdot H_{fs} \cdot H_{r_{ant}} \cdot H_r. \tag{16}$$

here H_{target} is the transfer function of the reference target used and H_{fs} from free space. With the calibration filter C_{ra} of the radar we get the calibration function for the antenna system,

$$C_{ant}(f) = (H_{t_{ant}} \cdot H_{r_{ant}})^{-1} = \frac{S_{ref} \cdot H_{fs} \cdot H_{target}}{S_{c_{ant}} \cdot C_{ra}}. \tag{17}$$

H_{target} and H_{fs} can be modelled and thus both can be sufficiently mitigated. S_{ref} and C_{ra} are well known and $S_{c_{ant}}$ is determined from the calibration measurement. Finally, with the radar transmit signal S_t we can describe the calibrated receive signal in time domain after the pulse compression by

$$s_{sat}(t) = \int_{-\infty}^{\infty} C_{ra} C_{ant} S_r S_t^*(f) e^{j2\pi f t} df \tag{18}$$

5 | SIMULATION RESULTS

In the following section, the theoretical performance of the imaging system, based on the parameters determined in the previous sections, is illustrated using simulation results. With respect to experimental measurements of the ISS as later described, prior simulation results for the imaging process are useful. The orbit and radar parameters of the simulation results are listed in Table 2. The orbital height was set to 400 km, being a typical average height for the ISS. Furthermore, the orbit was assumed to be circular, having thus a numerical eccentricity of zero. Using the orbital height together with the mean equatorial radius, one obtains the semi-major axis of the orbit. For the calculation of the orbital velocity the earth was assumed as point mass [33].

The maximum elevation angle of the ISS pass selected for the simulation is 51.1°. The equivalent imaging geometry resulting from the orbital parameters is shown in Figure 10. For clarity, the relative motion between the ISS and the radar system was converted into an equivalent movement of the radar system with a fixed ISS. Thus, the ISS is fixed in the origin of the coordinate system and the radar system moves along the space object on an equivalent path that corresponds to the relative motion of the real imaging geometry. The equivalent path of the radar system shows a slight curvature that is caused by the quadratic range migration of the ISS during the pass.

The vectors $\vec{x}$ and $\vec{y}$ in Figure 10 define the selected focal plane, which was chosen according to the alignment of the ISS

TABLE 1 Imaging of satellites in space imaging parameters.

Parameter	Value
Radar type	Pulse radar
Frequency band	X band
Centre frequency	10.2 GHz
Bandwidth	≤4.4 GHz
Transmit signal	Arbitrary
Pulse length	≤50 μs
Pulse repetition frequency	≤200 Hz
Pulse power at HPA output	8 kW
Transmit antenna diameter	9 m
Receive antenna I diameter	1.8 m
Receive antenna II diameter	1.8 m

TABLE 2 Simulation parameters.

Parameter	Value
Orbital height	400 km
Eccentricity	0
Elevation angle (max.)	51.1°
Frequency band	X band
Bandwidth	400 MHz/4.4 GHz
Azimuth integration angle	3°/23°
Pulse length	30 μs
Pulse repetition frequency	200 Hz
Signal type	Up-chirp

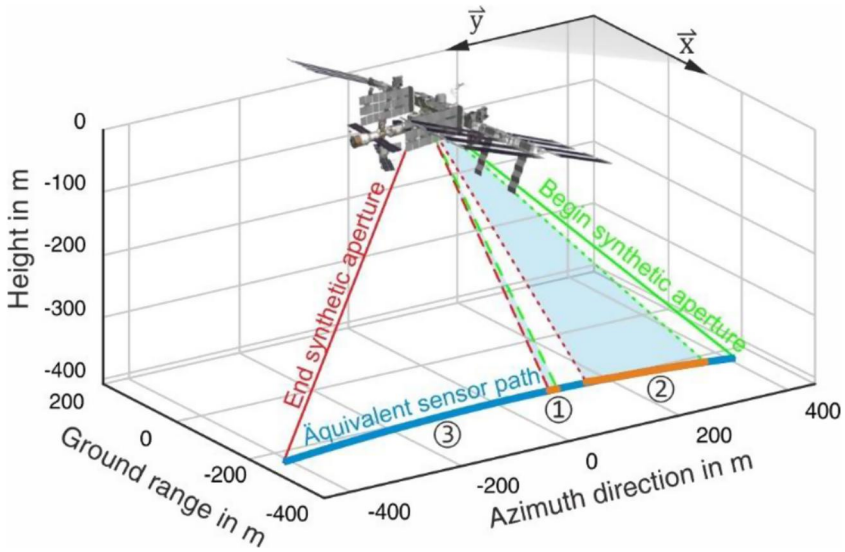

FIGURE 10 Illustration of different lengths of the synthetic aperture (SA) along the equivalent sensor path, resulting in an integration angle of 3° ①, 23° ②, and for the complete length of the international space station (ISS) path seen from imaging of satellites in space system (IoSiS) 78°③.

on its orbit in such a way that as many expected scattering centres as possible are within or, at least at a small distance from this plane. This minimises distortions in the subsequent radar image as well as defocusing due to the limited depth of focus that occurs with nonlinear sensor paths. [34].

Due to the orbit parameters, on which the imaging simulation is based, and the pass with a maximum elevation angle of 51.1°, an angle of incidence on the selected focal plane of about $\theta_F = 39°$ is obtained. As described in Section 2 this results in a degradation of the spatial resolution in the final radar image by the factor $1/\sin\theta_F = 1.59$ in range direction.

In the imaging geometry depicted, two smaller synthetic apertures of different lengths with an integration angle of $\varphi_{Az} = 3°$ and $\varphi_{Az} = 23°$ are highlighted.

Based on X band this corresponds to a spatial azimuth resolution of 40 and 4 cm, respectively. The shown segment of the ISS pass is within the range with an elevation angle greater than 37°, which would allow a very large SA and corresponds to an observation angle of 78°. The start of the SA is marked in green for all three specified integration angles; the end of the SA is marked in red.

The reflectivity map of the ISS used for the simulations is shown in Figure 11. The map was calculated on the basis of the 3D model also shown in Figure 11 (top) and is based on the mapping geometry described previously. The reflectivity map was calculated with a software tool developed in house, which enables the reflectivity determination of complex objects [36, 37], together with the 3D model of the ISS provided in [35].

The reflectivity map in Figure 11 bottom shows all scattering centres that appear within an integration angle of 23° of the corresponding SA in Figure 10. The reflectivity map was calculated for a frequency of 11 GHz, with a spatial sampling of the 3D model of 3 cm in all three spatial directions. Furthermore, when calculating the reflectivity map, all parts were assumed to be metallic. This simplified assumption of the imaging parameters and object properties (monochromatic and metallic surfaces) for determining the Reflectivity map was necessary to approximately determine the backscatter properties of such a large and, at the same time, complex object over a large angular range. When calculating the scattering effects, a distinction is made between the number of reflections on the object. These are colour coded in the illustration. The varying amplitude of the individual scattering centres is taken into account by the number of scattering centres at a spatial point and is therefore not recognisable in this representation. This only becomes apparent in the final radar image through superposition of the scattering centres during the ISAR image simulation. Due to the consideration of multiple reflections, individual scattering centres are also outside the structure of the ISS. As expected, most of the scatterers are located along the main truss segment of the ISS where a variety of modules and complex components are mounted.

The simulated ISAR images, which were processed based on the back-projection algorithm are shown in Figures 12 and 13 for two resolution cells of different sizes. The results show an ideal imaging simulation in which no external error influences, like atmospheric effects and errors in the orbit determination for instance, have any effect on the imaging process. With a bandwidth of 400 MHz and an integration angle of 3°, the size of the resolution cell is about 40 cm in both azimuth and range direction. The imaging geometry corresponds to section ① from the large SA shown in Figure 10. Due to the size of the ISS, the structure of the space station can be clearly seen even at this relatively low spatial resolution.

At the main truss segment, standing vertically in the image, on which a large number of individual additions are mounted, the overlapping of many individual scattering centres occurs. Thus, hardly any assignable details are recognisable in this area.

The lattice structure that is located between the solar collectors is recognisable, which indicates the alignment of the solar collectors. The solar collectors themselves are not visible, since they were aligned in such a way that they reflect the entire incident signal at a different angle and thus do not show any significant backscatter behaviour in this monostatic imaging geometry.

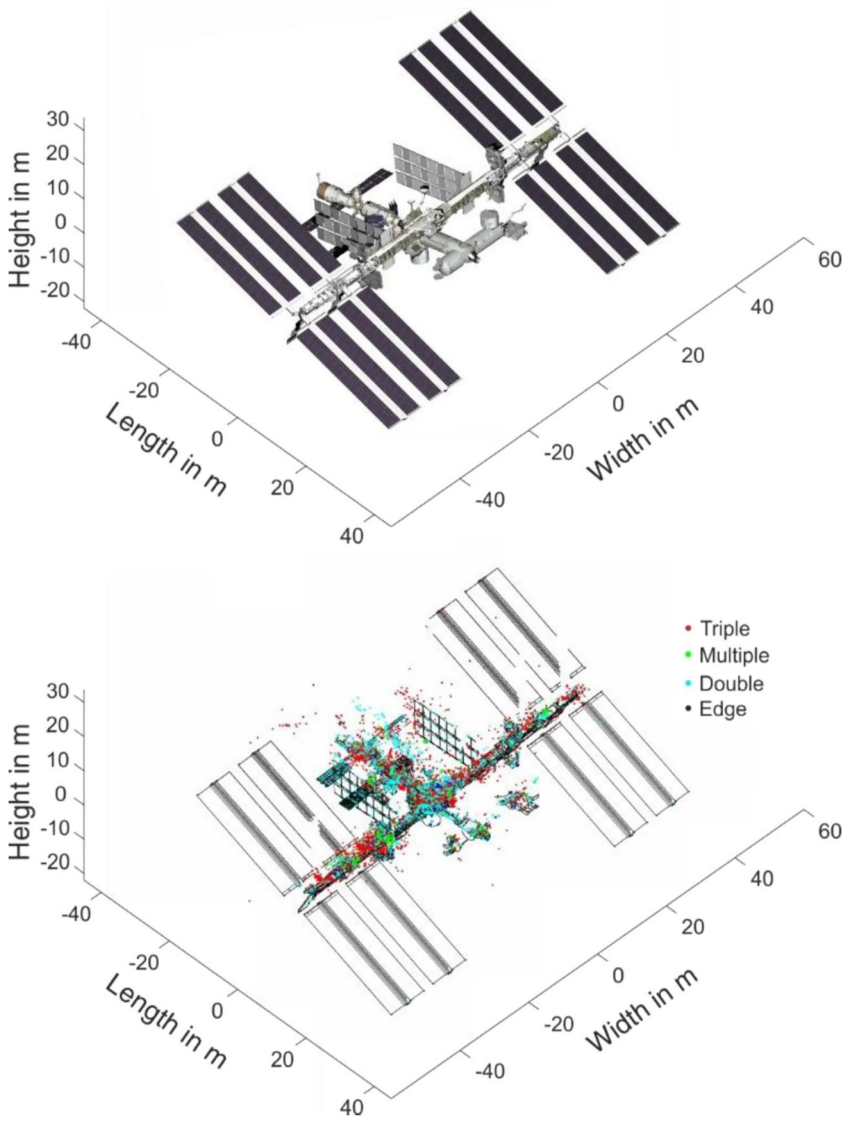

FIGURE 11 3D CAD model for the computation of the ideal reflectivity map of the international space station (ISS) (top) [35]. Colour coded reflectivity map of the ISS (down).

If now the spatial resolution is improved to about 3.5 cm, the structure is reproduced in extremely great detail. In this range of spatial resolution, single scattering centres with very strong radar backscatter cross-sections occur. This results in a significant increase in the dynamic range of the radar image. To maintain the ability to display scatter centres of lower amplitude in this ISAR image, the dynamic range in Figure 13 was adjusted accordingly. The imaging geometry corresponds to section ② from the large SA shown in Figure 10. The edges of the solar collectors on both sides of the station are clearly visible. Due to the alignment in connection with the projection onto the image plane, however, the solar collectors are slightly distorted and thus they appear smaller than they actually are.

An enlarged illustration of the highlighted (dashed rectangle) module is depicted in Figures 14 and 15. In the low-resolution image (40 cm) only the contour of the module and the solar panels are recognisable. On the high-resolution image (3.5 cm), details on the cylindrical module and even the individual sections of the solar modules can be seen. On the far right of the two images, other structures of the ISS can be seen that do not belong to the rear module. The comparison shows how important the resolution is for a proper evaluation of the satellite structures. A resolution in the lower centimetre range and even below is absolutely necessary.

6 | EXPERIMENTAL RESULTS

6.1 | Processing steps

To obtain a well-focused ISAR image, a couple of subsequent signal processing steps have to be carried out as indicated in Figure 16. Due to the large range migration of a passing satellite, the receive window of length 5 km has to be shifted successively to the actual radar distance to the satellite. In this way, a large range area can be covered with a small receive window, leading to considerably reduced amount of sampled data. During a typical satellite pass roughly 130 receive windows are required with an overlap of 1.5 km for two adjacent windows. Hence the first processing steps are the allocation of the pulses to their

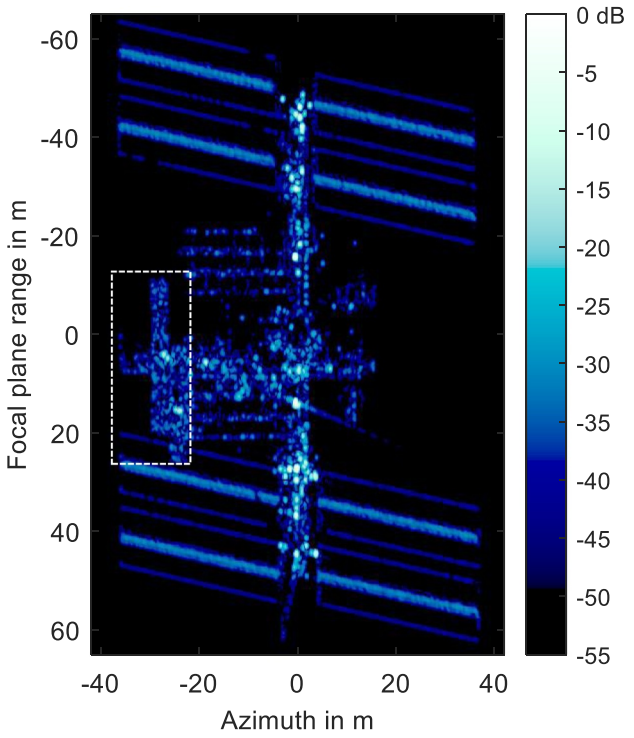

FIGURE 12 Simulation result of the international space station (ISS) using an integration angle of 3° (corresponds to ① in Figure 10) and a bandwidth of 400 MHz. The corresponding spatial resolution is 40 cm.

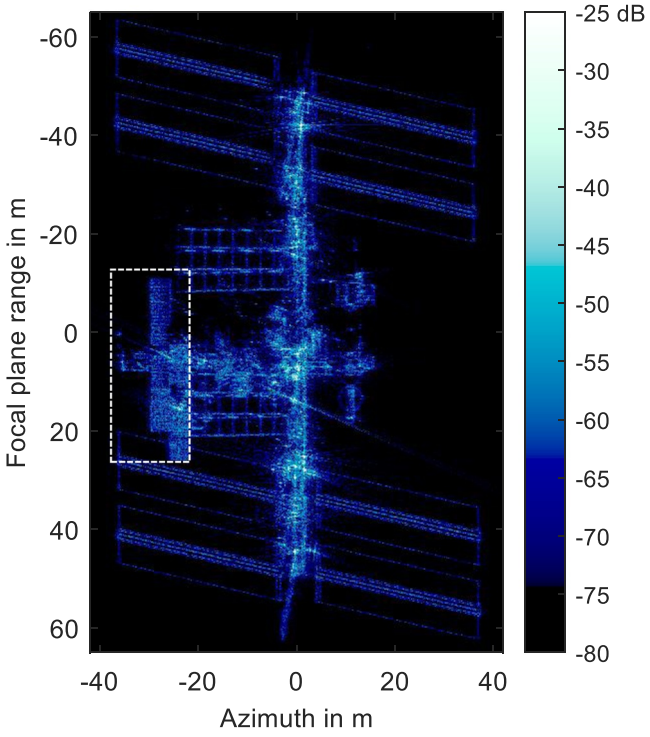

FIGURE 13 Simulation result of the international space station using an integration angle of 23° (corresponds to ② in Figure 10) and a bandwidth of 4.4 GHz. The corresponding spatial resolution is 3.5 cm.

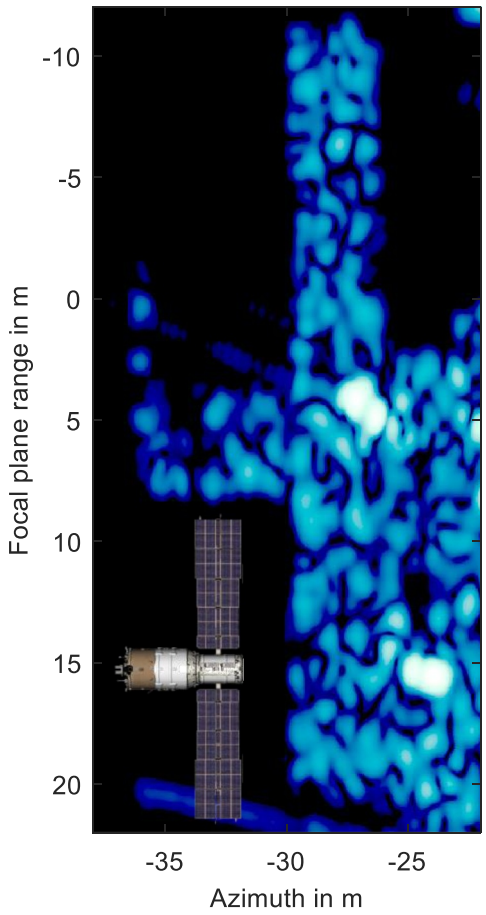

FIGURE 14 Enlarged illustration of the Zvesda module with a spatial resolution of 40 cm.

corresponding receive window and a basic range correction. Additionally, errors, based on meteorological parameters such as the influence of the troposphere, leading to a frequency independent range error, and the ionosphere, leading to a frequency dependent range error, are approximatively compensated [29, 38, 39]. Considering nearly circular orbits (Eccentricity ≈ 0) at orbital altitudes between 400 and 1500 km above the earth surface, the corresponding orbital velocities are between about 7.67 km/s and 7.15 km/s [40]. These high orbital speeds result in a considerable Doppler shift and hence produce a significant range cell migration, resulting in defocusing of the range profiles in high-resolution radar, if not compensated. However, by mitigating the known Doppler shift this degrading effect can be eliminated. The Doppler shift must be calculated and considered for each individual frequency in the signal spectrum and not only for the centre frequency.

Next the non-ideal frequency transfer function of the whole radar system is compensated in two steps (see also Section 4.2). First this is done for Tx and Rx antennas by using calibration measurements from a reference target like a trihedral reflector with a well-known response. Then the transfer function of the radar electronics itself is corrected using a special calibration procedure. This procedure is carried out

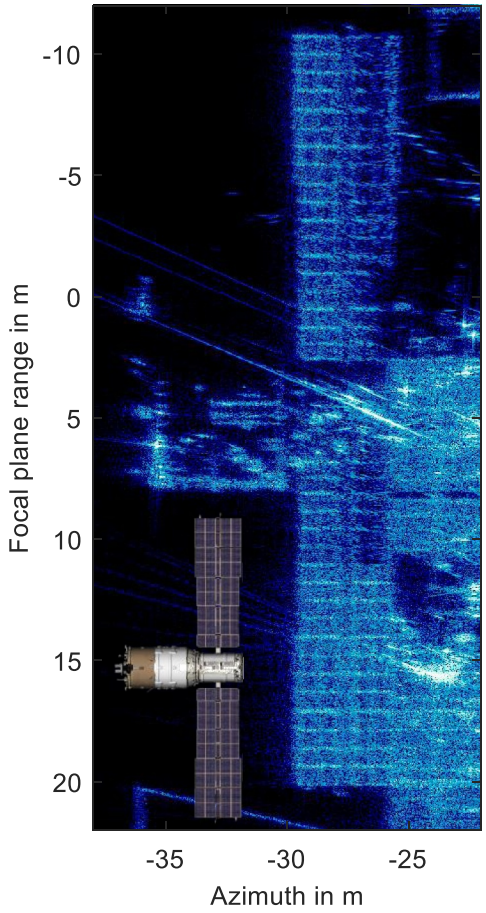

FIGURE 15 Enlarged illustration of the Zvesda module with a spatial resolution of 3.5 cm.

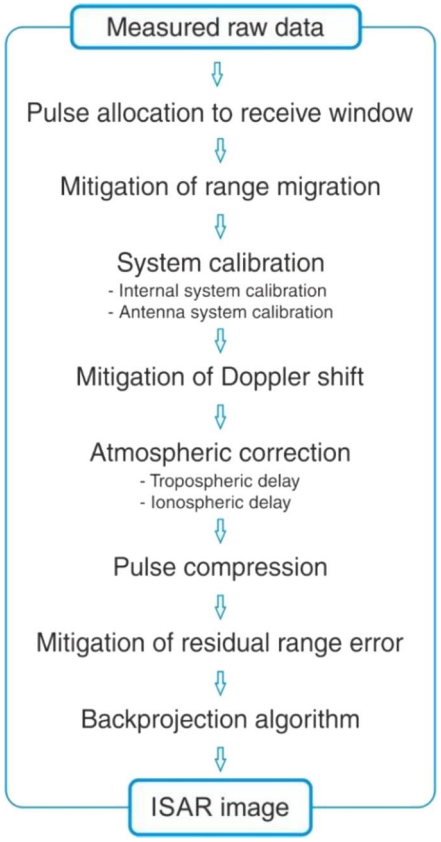

FIGURE 16 Signal processing steps for the imaging of satellites in space basic inverse synthetic aperture radar processor.

shortly before and after each ISAR measurement using a well-known line segment as calibration path. Since for the Tx signal a linearly frequency-modulated pulse (LFM chirp) is usually used, the next processing step is a pulse compression, focussing the range profiles in range direction.

However, at the end of the previous processing procedure, often a range migration can be identified. This range error mainly is caused by residual errors of orbit prediction and can be in the order of several hundred metres. At the time of this writing, IoSiS does not have the possibility to auto track a space object. Thus, the knowledge of the satellite paths is crucial in order to obtain the trajectory information required for the ISAR processing. Presently the necessary orbit predictions are performed using publicly available Two-Line-Element (TLE) data, which only allow predictions within a specific accuracy. In addition, small parts of the residual range errors can also be caused by limited compensation of atmospheric range delay. As a consequence, an additional mitigation of the residual range error has to be performed. This is done by extracting a robust point target in the focused range profiles, which can be extracted over a sufficiently wide range of azimuth angles. Using this, a first linear range correction is carried out and afterwards, if necessary, an additional quadratic correction is applied.

It is foreseen that this residual range error will be mitigated by a dedicated autofocus algorithm [41]. Finally, for ISAR processing a back-projection algorithm is applied [27].

6.2 | Measurement result I

Figure 17 shows an image of the ISS obtained with the currently highest possible bandwidth of 2.8 GHz, which was used for experimental purposes and corresponds to a theoretical range resolution of 5.4 cm [20]. The previously described maximum bandwidth of 4.4 GHz could not be fully utilised due to possible interference with neighbouring communication systems. However, note that IoSiS is allowed to operate such large bandwidth by given licence for experimental operation of German frequency regulation authority. Further measurement parameters are listed in Table 3.

For image formation a classic back-projection of the individual range profiles onto a Cartesian grid was used. The focal plane was placed in the main plane of the ISS. In this way distortions in the subsequent radar image as well as defocusing caused by the limited depth of focus are minimised [34]. Fortunately, the solar panels were also aligned with the focal plane during the measurement. This is not always necessarily the case, since they are always tracked by the incident sunlight and thus use a different position depending on the position of

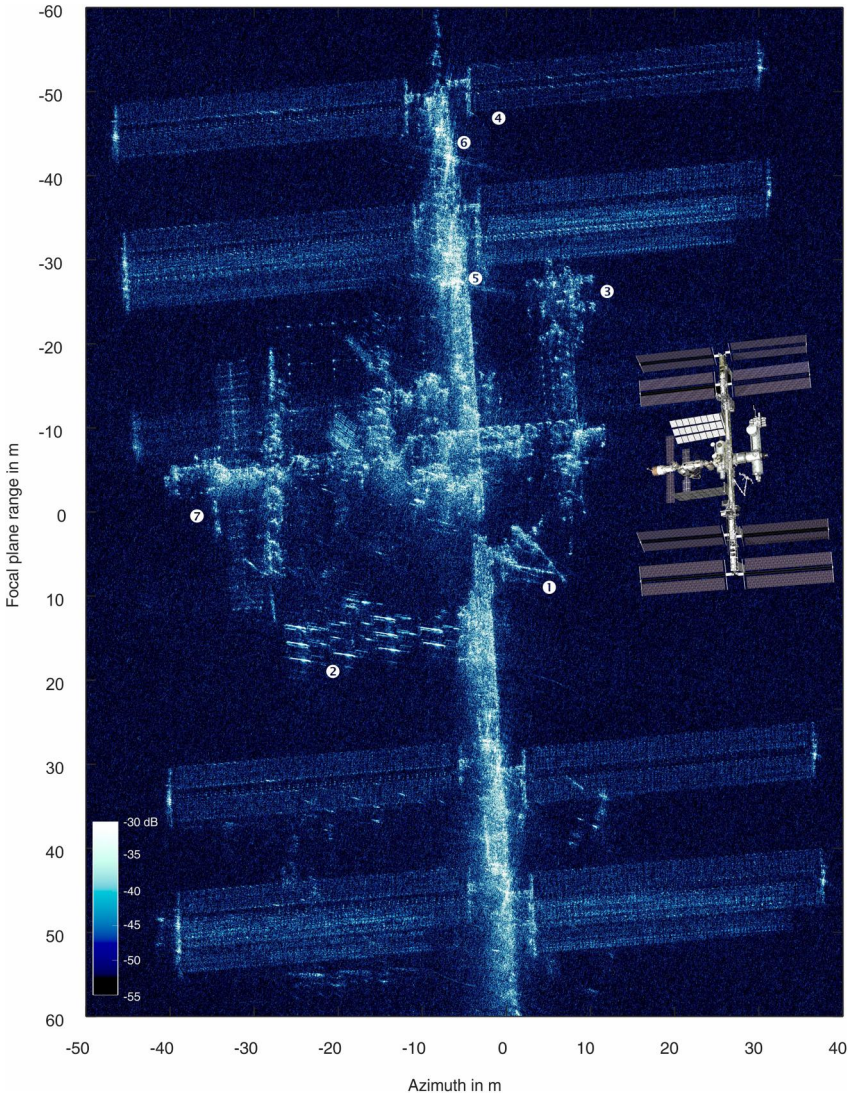

FIGURE 17 Measured inverse synthetic aperture radar image of the international space station using a bandwidth of 2.8 GHz and an azimuth integration angle of 28°, resulting in a range resolution of 5.4 cm and a theoretical azimuth resolution of 2.8 cm. The image was focused in a pre-defined focal plane using a back-projection algorithm. The focal plane was chosen according to the alignment of the main ISS truss segment. With a mean incident angle of 65° the focal plane range resolution is approximately 6 cm [20].

TABLE 3 Measurement parameters.

Parameter	Value
Radar location (lat/long)	47.8809/11.0818 deg
Object (Cospar ID)	ISS (1998-067A)
Frequency band	X band
Bandwidth	2.8 GHz
Azimuth integration angle	28 deg
Pulse length	32 μs
Pulse repetition frequency	190 Hz
Azimuth sampling interval (min.)	0.0048 deg
Unambiguous range (azimuth)	160 m
Signal type	Up-chirp
Range (min./max.)	605/709 km
Number of pulses	9000
Spectrum weighting (range)	Rectangular
Spectrum weighting (azimuth)	Rectangular

the sun. In the azimuth direction, 9000 available range profiles were used for focussing, which in this case corresponds to an integration angle of 28° or, equivalently, a theoretical azimuth resolution of 2.8 cm. However, this resolution can only be achieved if a scattering centre makes a significant contribution to amplitude and phase over this large angular range.

Thus, with regard to the spatial resolution that can be achieved in the azimuth direction, the size of the resolution cell can no longer be inferred directly from the angle width at these large integration angles. Here the decisive advantage of the large integration angle is not so much the spatial resolution achieved, but rather the appearance of as many scattering centres as possible. The large integration angle has the positive effect that more scattering centres become visible for an image acquisition than with smaller integration angles.

Like the simulation results have already shown, a few robust scattering centres have a significantly larger amplitude than the rest of the structure. Therefore, the depicted ISAR image is normalised to −30 dB. Otherwise, the strong robust scattering centres would severely limit the visibility of low-intensity scattering.

A large number of details can be seen in the central area of the space station due to the high spatial resolution and the large integration angle. The 17 m long mobile robot arm (❶) with a diameter of 38 cm for transporting payloads shows a conspicuous backscatter behaviour. Even though the robot arm is made of carbon fibre reinforced epoxy resin, a non-metal, and a cover of an aramid fibre layer for protection, it exhibits a significant backscatter amplitude. Furthermore, the heat radiators (❷) can be identified in the radar image, which consist of several unfolded surfaces. The edges of the individual surface elements are clearly visible in the image. The area of the KIBO module (❸) also shows a high level of detail. In addition to the cylindrical module, the outer platform can also be seen here and the individual experimental canisters mounted on it are clearly resolved. The eight large 35-m solar panels are visible and show no significant azimuth distortion, suggesting they were positioned in the focal plane region. In the range direction, on the other hand, a clear compression can be seen (most clearly on the solar panel at the top right ❹). This shows that the surface normal of the focal plane and the solar panels were not parallel during acquisition.

An enlarged view of the rear ISS module is depicted in Figure 18 in comparison to the 3D model. As already seen in the simulations, the high spatial resolution allows a detailed analysis of the structure. For example, the solar modules and even the subsections of the modules are resolved. On the far right of the image are other structures of the ISS that do not belong to the module.

6.3 | Point spread function analysis

In order to verify the achieved spatial resolution, robust scatterers has been analysed. The ISAR image analysis of the ISS has shown that the structure of the ISS contains several parts which act as strong robust scatterers. After the image processing the peak amplitudes of these scatterers are up to 40 dB higher than the average amplitude of the other parts of the structure. The location of two of these robust scatterers is marked with ❺ and ❻ in Figure 17. This section is shown enlarged in Figures 19 and 20, with an appropriate adjusted dynamic range. The image shows the well-focused robust scatterer. The residual structure around the scatterer cannot be identified because the amplitude is mainly 30 dB lower with respect to the peak amplitude of the robust scatterers. Figure 21 shows the corresponding range and azimuth profiles, respectively. No weighting was applied in the frequency domain. In the focal plane range the half power beam width (HPBW) of both point spread functions is 6.8 cm and corresponds nearly to the theoretical value. It must be mentioned, that the focal plane range resolution is slightly worse than the slant range resolution due to the projection angle between the radar line of sight and the focal plane. The peak sidelobe ratio (PSLR) is not perfectly symmetrical indicating a residual phase error or an influence of the adjacent scatterers. Nevertheless, the PSLR is near the theoretical value of 13.3 dB.

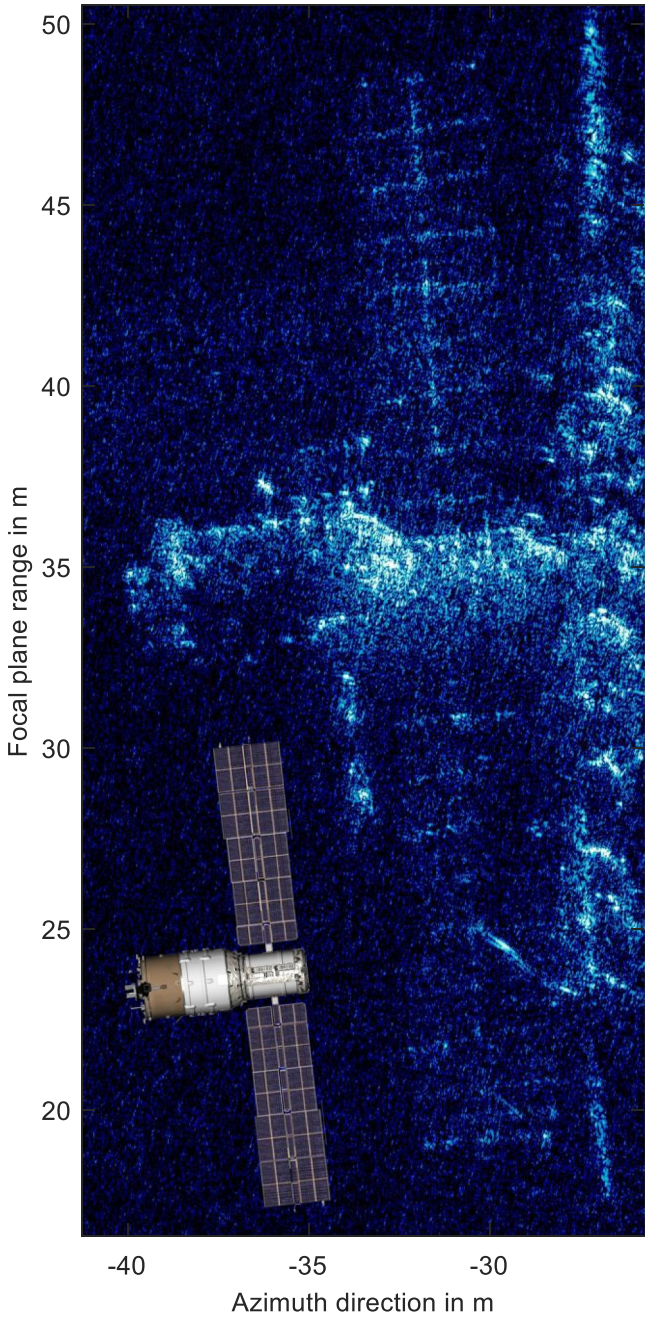

FIGURE 18 Enlarged illustration of the Zvesda module ❼.

The integrated sidelobe ratio (ISLR) defines ratio the between the energy in the sidelobes and the energy in the main lobe.

In azimuth direction the HPBW and spatial resolution is 3.5 cm, respectively. This demonstrates that nearly the very high theoretical resolution of 2.8 cm can be achieved and indicates that the robust scatterers exhibit a low angle dependent RCS. However, investigations of the range profiles have shown that the RCS of both scatterers is not visible over the full integration angle of 28°. As a result, the theoretical resolution values are reduced as mentioned above. The large integration angle leads to a very high side lobe suppression and thus to a good ISLR

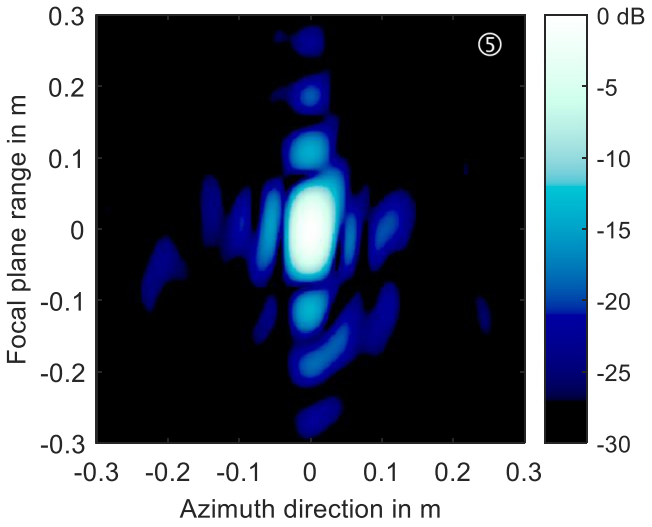

FIGURE 19 Isolated image section of a robust scatterer of the international space station (ISS) inverse synthetic aperture radar (ISAR) image for verification of the achieved spatial resolution.

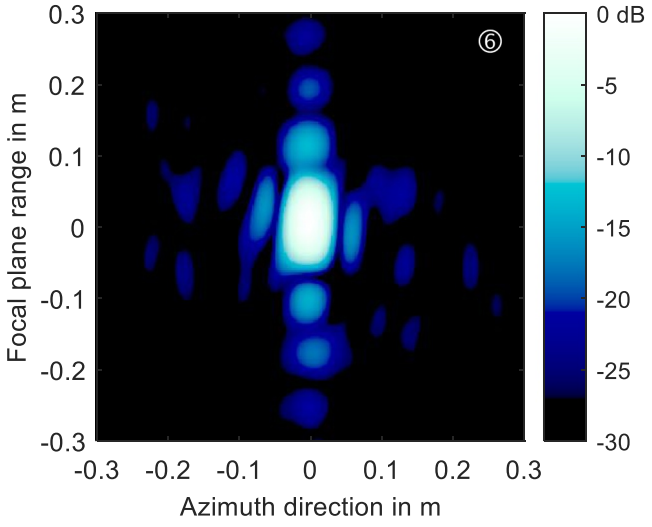

FIGURE 20 Isolated image section of a robust scatterer of the international space station (ISS) inverse synthetic aperture radar (ISAR) image for verification of the achieved spatial resolution.

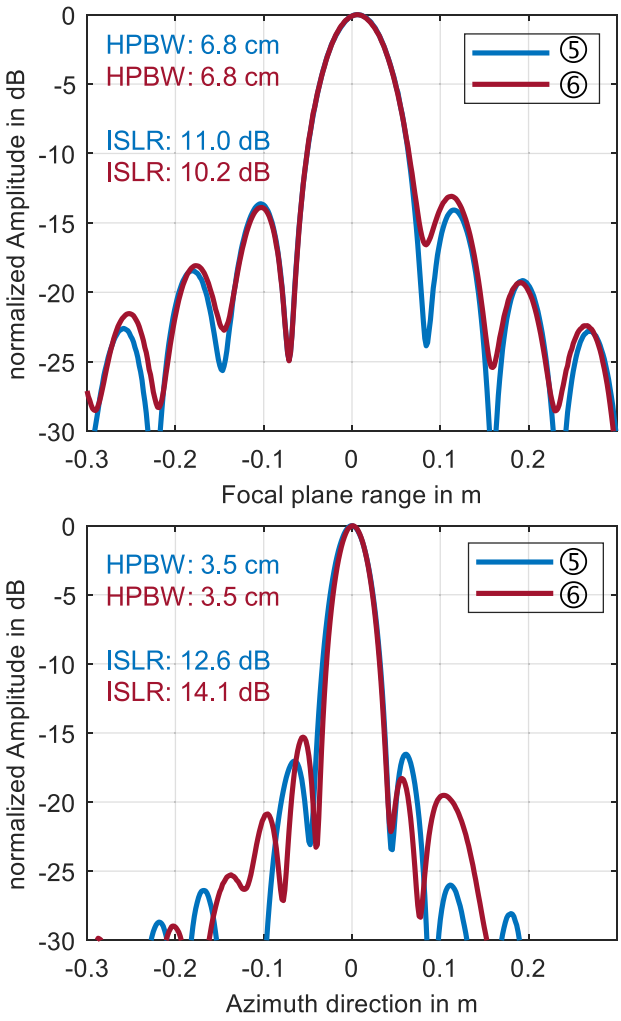

FIGURE 21 Range and azimuth profile of two isolated robust scatterers shown in Figures 19 and 20. The half-power beam width (HPBW) is 6.8 cm in the focal plane range and 3.5 cm in azimuth direction.

value. A slight asymmetry can be seen in the PSLR, indicating a non-ideal phase response, which could be due to the influence of the neighbouring scatterers. But this is acceptable given the large integration angle.

This analysis of the point spread function is not ideal due to the surrounding scatterers in the background and because the true structure of the point target is not known. However, the analysis shows that the expected very high spatial resolution is achieved with the presented radar system. In order to do a more precise evaluation of the achievable spatial resolution and further image parameters a completely isolated angle independent well-known target should be used.

Nevertheless, this measurement result shows impressively the successive development and implementation of processing and error correction steps being necessary to achieve a very high-quality image in both range and azimuth direction.

6.4 | Measurement result II

A further measurement result is illustrated in Figure 22. It shows the ISS from a different perspective than the image shown in Figure 17. In particular, the solar arrays are rotated so that they do not appear in the ISAR image. Only the structure at the end of each solar panel can be identified, which makes it possible to determine the position of the panel. The image was processed using 6400 pulses, which, based on the geometry of the measurement, corresponds to an integration angle of 22.2°. The comparison with the image in Figure 17 shows that the angle of incidence and the resulting perspective can have a significant effect on the radar image. As a result, different perspectives show different parts of the object.

An enlarged view of the front part of the ISS is shown in Figure 23. For the purpose of comparison, a 3D CAD model

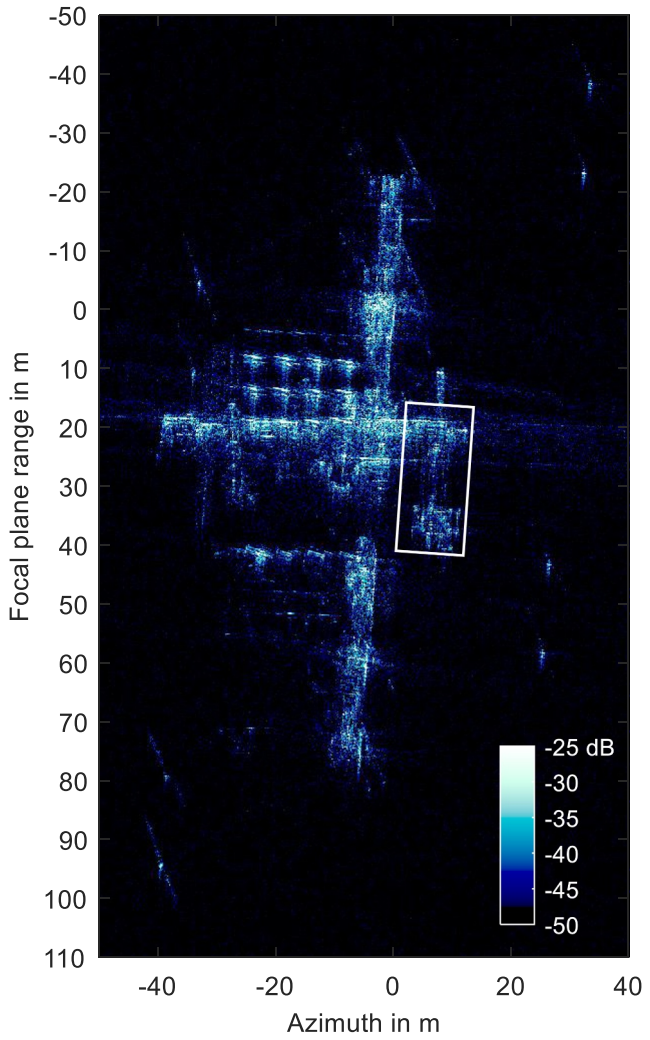

FIGURE 22 Measured inverse synthetic aperture radar (ISAR) image of the international space station (ISS).

of this section is also shown in the illustration [35]. The section contains a cylindrical module of 11 m in length with an attached exposed facility for experiments. The radar image shows that the module appears to have small structures on the cylindrical surface that are parallel to the longitudinal axis of the module. These structures scatter the incident field and lead to a plastic impression of the tube in the radar image. In the upper part of the image, strong reflections from other cylindrical modules can be seen, arranged almost perpendicular to the radar's line of sight. The exposed facility shows strong backscattering behaviour in the lower part of the image. The radar image shows that the exposed facility is made up of a complex structure that differs from the CAD model. In addition, the radar image makes it possible to identify the various smaller containers that are used for the experiments. As indicated by the orange rectangle, it is easy to see that the lower left slot was obviously fitted with a container during the measurement, whereas the CAD model does not show this container.

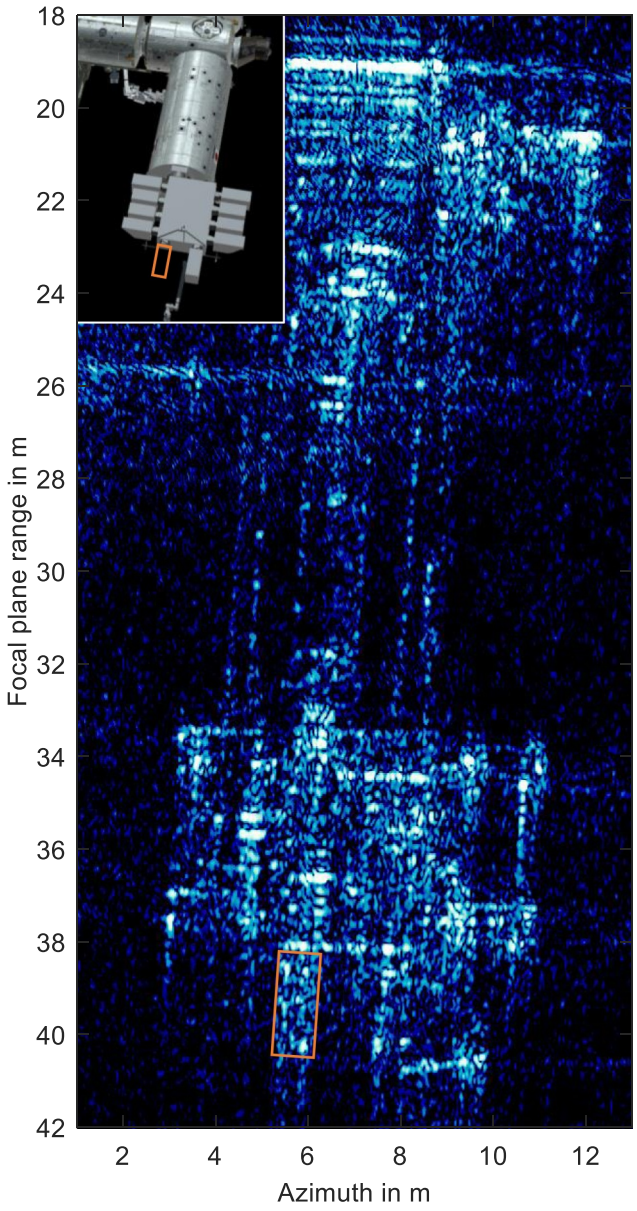

FIGURE 23 Enlarged illustration of the image section highlighted in Figure 22 in comparison with the 3D CAD model of this section of the international space station (ISS).

7 | CONCLUSION

In order to address the future demands of high-performance space surveillance, DLR is performing theoretical investigations on advanced radar technology and has additionally constructed an experimental satellite imaging radar called IoSiS. As research with IoSiS is focused on developing new imaging concepts and improving image quality, IoSiS is designed as a pure imaging radar and does not have a tracking capability. This paper is therefore intended to comprehensively communicate and illustrate the technological steps necessary for the development and successful operation of advanced radar-based satellite imaging system. The processing steps and error correction

strategies developed and presented enable very high-quality imaging of objects in space, which in turn enables detailed analysis of their structure. Based on a modelled reflectivity distribution of the ISS, simulated results of the IoSiS system simulator software show the potential of such a radar system, mainly expressed by the high spatial resolution according to its actually used system bandwidth of 2.8 GHz. Further investigation results show that even higher frequencies in the millimetre-wave domain are attractive for future high-performance imaging of LEO objects.

The shown measurement results of the ISS demonstrates the very high performance of the developed experimental radar system and proves the introduced and successfully implemented error strategies to be correct and efficient.

The executed and ongoing research supports the investigation on an intended future multifunctional radar-based satellite imaging system using a new imaging concept with distributed apertures. For this reason, the present IoSiS system has been implemented as a multi-channel radar system, that is, one transmission channel connected to a larger main dish and two receive channels using two separated smaller receive antennas, being suitable for both bi- and multi-static imaging in future. However, the configuration presently acts as a quasi mono-static radar system, but it shall serve as a basis for further research on the new concept.

AUTHOR CONTRIBUTIONS

Simon Anger: Conceptualization; data curation; formal analysis; investigation; software; validation; visualization; writing—original draft. **Matthias Jirousek**: Data curation; investigation; writing—original draft; writing—review and editing. **Stephan Dill**: Conceptualization; investigation; validation; writing—original draft; writing—review and editing. **Timo Kempf**: Formal analysis; software; writing—review and editing. **Markus Peichl**: Conceptualization; funding acquisition; project administration; supervision; writing—review and editing.

ACKNOWLEDGEMENTS

The authors thank Martin Häusler and his colleagues from the DLR satellite ground station for supporting this research. This work has been partially supported by Federal Office of Bundeswehr Equipment, Information Technology and In-Service Support.

Open Access funding enabled and organized by Projekt DEAL.

CONFLICT OF INTEREST STATEMENT

The authors declare no conflict of interest.

DATA AVAILABILITY STATEMENT

The data that support the findings of this research are partly available from the corresponding author upon reasonable request.

ORCID

Simon Anger https://orcid.org/0000-0002-6332-9781

REFERENCES

1. ESA's Annual Space Environment Report: Esa Space Debris Office, GEN-DB-LOG-00288-OPS-SD, Issue 7.0, Darmstadt. Germany (2023)
2. United Nations Office for Outer Space Affairs: Online Index of Objects Launched into Outer Space (2023). https://www.unoosa.org/oosa/osoindex/search-ng.jspx?lf_id=
3. Karamanavis, V., et al.: Characterization of deorbiting satellites and space debris with radar. Adv. Space Res. 72(8), 3269–3281 (2023). https://doi.org/10.1016/j.asr.2023.07.033
4. Avent, R.K., Shelton, J.D., Brown, P.: The ALCOR C-band imaging radar. IEEE Antenn. Propag. Mag. 38(3), 16–27 (1996). https://doi.org/10.1109/74.511949
5. Abouzahra, M.D., Avent, R.K.: The 100-kW millimeter-wave radar at the Kwajalein Atoll. IEEE Antenn. Propag. Mag. 36(2), 7–19 (1994). https://doi.org/10.1109/74.275546
6. Abouzahra, M.: The millimeter wave radar at Kwajalein missile range. In: SPIE Int. Conf. on Millimeter and Submillimeter Waves and Applications II, pp. 2258 (1995)
7. Ender, J., et al.: Radar techniques for space situational awareness. In: 2011 12th International Radar Symposium (IRS), pp. 21–26 (2011)
8. Czerwinski, M.G., Usoff, J.M.: Development of the haystack ultra-wideband satellite imaging radar. MIT Lincoln Laboratory Journal 21(1), 28–44 (2014)
9. Stambaugh, J.J., Lee, R.K., Cantrell, W.H.: The 4 GHz bandwidth millimeter-wave radar. Linc. Lab. J. 10(2) (2012)
10. Wilden, H., et al.: GESTRA—a phased-array based surveillance and tracking radar for space situational awareness. In: 2016 IEEE International Symposium on Phased Array Systems and Technology (PAST), pp. 1–5 (2016). https://doi.org/10.1109/ARRAY.2016.7832621
11. Reising, C., et al.: GESTRA - upgrading to future distributed phased array radar networks for space surveillance. In: 2022 IEEE International Symposium on Phased Array Systems and Technology (PAST), pp. 1–8. Waltham (2022). https://doi.org/10.1109/PAST49659.2022.9975037
12. Ionescu, L., et al.: Development of the Romanian radar sensor for space surveillance and tracking activities. Sensors 22(9), 3546 (2022). https://doi.org/10.3390/s22093546
13. William, W.C., Joseph, T.M., Robert, M.O.: Wideband radar for ballisitic missile defense and range Doppler imaging of satellite. MIT Lincoln Laboratory Journal 12(2), 267–280 (2000)
14. Chatters, E.P., Crothers, B.J.: Space Surveillance Network, AU-18 Space Primer, pp. 249–258. Air University Press (2009). JSTOR
15. Anger, S., et al.: IoSiS—a high performance experimental imaging radar for space surveillance. In: 2019 IEEE Radar Conference (RadarConf), vol. 2019, pp. 1–4. https://doi.org/10.1109/RADAR.2019.8835824
16. Anger, S., et al.: Research on advanced space surveillance using the IoSiS radar system. In: EUSAR 2021; 13th European Conference on Synthetic Aperture Radar, pp. 1–4 (2021)
17. Anger, S., et al.: ISAR imaging of satellites in space—simulations and measurements. In: 2019 20th International Radar Symposium (IRS), pp. 1–6 (2019). https://doi.org/10.23919/IRS.2019.8768095
18. Anger, S., et al.: Imaging of satellites in space (IoSiS): challenges in image processing of ground-based high-resolution ISAR data. In: Proc. SPIE 10633. Radar Sensor Technology XXII 106330L(4) (2018)
19. Lazio, J., et al.: Ground-based planetary radars: current and future prospects in the cislunar arena. In: Advanced Maui Optical and Space Surveillance Technologies Conference (AMOS). Maui (2022)
20. Anger, S.: Mikrowellenmessverfahren zur erdgebundenen hochgenauen Abbildung von Weltraumobjekten auf erdnahen Umlaufbahnen. Ph.D. dissertation. University Ulm, Ulm, Germany (2020)
21. Kempf, T.: Extraktion von objektspezifischen Radarsignaturen am Turmdrehstand. Ph.D. Dissertation. Bundeswehr University, Munich (2020)
22. Gurrisi, C., et al.: Space station control moment gyroscope lessons learned. In: Proceedings of the 40th Aerospace Mechanisms Symposium (2012)
23. Rosebrock, J.: Absolute attitude from monostatic radar measurements of rotating objects. In: IEEE Transactions on Geoscience and Remote

Sensing, vol. 49, pp. 3737–3744 (2011). https://doi.org/10.1109/TGRS.2011.2159727
24. Kark, K.: Antennen und Strahlungsfelder. Vieweg+Teubner Verlag, Wiesbaden (2011)
25. Vehmas, R., Neuberger, N.: Inverse synthetic aperture radar imaging: a historical perspective and state-of-the-art survey. IEEE Access 9, 113917–113943 (2021). https://doi.org/10.1109/ACCESS.2021.3104799
26. Ulander, L.M.: Impulse response function for ultra-wideband SAR. In: EUSAR 2014; 10th European Conference on Synthetic Aperture Radar, pp. 1–4 (2014)
27. Mensa, D.: High resolution radar cross-section imaging. Artech House (1991)
28. Vallado, D.A.: Fundamentals of Astrodynamics and Applications. Springer, New York (2007)
29. ITU: Attenuation by atmospheric gases. In: International Telecommunication Union, Recommendation ITU-R P.676–8 (2009)
30. Haas, A., Peichl, M. and Anger, S.: Design of wide-band corrugated feed horn for reflector antenna in radar applications. In: 2016 German Microwave Conference (GeMiC), pp. 65–68 (2016). https://doi.org/10.1109/GEMIC.2016.7461557
31. Jirousek, M., et al.: Characteristics of the high-performance highly digitized multi-purpose radar system GigaRad: system concept, system correction and calibration, applications. In: 2018 11th German Microwave Conference (GeMiC), vol. 2018, pp. 395–398. https://doi.org/10.23919/GEMIC.2018.8335113
32. Jirousek, M., et al.: GigaRad—a multi-purpose high-resolution ground-based radar system: system concept, error correction strategies and performance verification. In: 2014 11th European Radar Conference, vol. 2014, pp. 149–152. https://doi.org/10.1109/EuRAD.2014.6991229
33. Giese, R.H.: Weltraum Forschung I. Bibliographisches Institut AG, Mannheim (1966)
34. Kempf, T., Anglberger, H., Suess, H.: Depth-of-focus issues on space-borne very high resolution SAR. In: 2012 IEEE International Geoscience and Remote Sensing Symposium, pp. 7448–7451 (2012). https://doi.org/10.1109/IGARSS.2012.6351939
35. NASA JOHNSON SPACE CENTER: International Space Station (2011). https://nasa3d.arc.nasa.gov/detail/iss-hi-res
36. Anglberger, H., Speck, R., Suess, H.: Applications of simulation techniques for high resolution SAR systems. In: 2012 IEEE International Geoscience and Remote Sensing Symposium, pp. 5187–5190 (2012). https://doi.org/10.1109/IGARSS.2012.6352441
37. Anglberger, H.: Simulation und Analyse von SAR-Signaturen mit hoher Auflösung. Ph.D. dissertation. Bundeswehr University, Munich (2015)
38. ITU: Reference Standard Atmosphere, International Telecommunication Union, Recommendation ITU-R P835–6 (2017)
39. ITU: Propagation Data and Prediction Methods Required for the Design of Earth-Space Telecommunication Systems, Recommendation ITU-R P618–10 (2019)
40. Montenbruck, O., Gill, E.: Satellite Orbits—Models, Methods, and Applications. Springer-Verlag, Heidelberg (2001)
41. Wahl, D.E., et al.: Phase gradient autofocus-a robust tool for high resolution SAR phase correction. In: IEEE Transactions on Aerospace and Electronic Systems, vol. 30, pp. 827–835 (1994). https://doi.org/10.1109/7.303752

How to cite this article: Anger, S., et al.: High-resolution inverse synthetic aperture radar imaging of satellites in space. IET Radar Sonar Navig. 1–20 (2023). https://doi.org/10.1049/rsn2.12505